

1 Dealing with Spatial Heterogeneity in Pointwise to Gridded 2 Data Comparisons

3
4 Amir H. Souri^{1*}, Kelly Chance¹, Kang Sun^{2,3}, Xiong Liu¹, and Matthew S. Johnson⁴

5
6 ¹Atomic and Molecular Physics (AMP) Division, Harvard-Smithsonian Center for Astrophysics,
7 Cambridge, MA, USA

8 ²Department of Civil, Structural and Environmental Engineering, University at Buffalo, Buffalo, NY, USA

9 ³Research and Education in Energy, Environment and Water Institute, University at Buffalo, Buffalo, NY,
10 USA

11 ⁴Earth Science Division, NASA Ames Research Center, Moffett Field, CA, USA

12
13 *Corresponding author: ahsouri@cfa.harvard.edu

14 Abstract

15 Most studies on validation of satellite trace gas retrievals or atmospheric chemical transport models
16 assume that pointwise measurements, which roughly represent the element of space, should
17 compare well with satellite (model) pixels (grid box). This assumption implies that the field of
18 interest must possess a high degree of spatial homogeneity within the pixels (grid box), which may
19 not hold true for species with short atmospheric lifetimes or in the proximity of plumes. Results of
20 this assumption often lead to a perception of a nonphysical discrepancy between data, resulting
21 from different spatial scales, potentially making the comparisons prone to overinterpretation.
22 Semivariogram is a mathematical expression of spatial variability in discrete data. Modeling the
23 semivariogram behavior permits carrying out spatial optimal linear prediction of a random process
24 field using kriging. Kriging can extract the spatial information (variance) pertaining to a specific
25 scale, which in turn translating pointwise data to a gridded space with quantified uncertainty such
26 that a grid-to-grid comparison can be made. Here, using both theoretical and real-world
27 experiments, we demonstrate that this classical geostatistical approach can be well adapted to
28 solving problems in evaluating model-predicted or satellite-derived atmospheric trace gases. This
29 study suggests that satellite validation procedures using the present method must take kriging
30 variance and satellite spatial response functions into account. We present the comparison of Ozone
31 Monitoring Instrument (OMI) tropospheric NO₂ columns against 11 Pandora Spectrometer
32 Instrument (PSI) systems during the DISCOVER-AQ campaign over Houston. The least-squares
33 fit to the paired data shows a low slope ($OMI=0.76\times PSI+1.18\times 10^{15}$ molecules cm⁻², $r^2=0.67$)
34 which is indicative of varying biases in OMI. This perceived slope, induced by the problem of
35 spatial scale, disappears in the comparison of the convolved kriged PSI and OMI
36 ($0.96\times PSI+0.66\times 10^{15}$ molecules cm⁻², $r^2=0.72$) illustrating that OMI possibly has a constant
37 systematic bias over the area. To avoid gross errors in comparisons made between gridded data
38 versus pointwise measurements, we argue that the concept of semivariogram (or spatial auto-
39 correlation) should be taken into consideration, particularly if the field exhibits a strong degree of
40 spatial heterogeneity at the scale of satellite and/or model footprints.

41

42 **1. Introduction**

43 Most of the literature on validation of satellite trace gas retrievals or atmospheric chemical
44 transport models assume that geophysical quantities within a satellite pixel or a model grid box
45 are spatially homogeneous. Nevertheless, it has long been recognized that this assumption can
46 often be violated; spatially coarse atmospheric models or satellites are often not able to represent
47 features, nor physical processes, transpiring at fine spatial scales. Janjic et al. [2016] used the term
48 of *representation error* to describe this complication. They posit that this problem is a result of
49 two combined factors: unresolved spatial scales and physiochemical processes. To elaborate on
50 this definition, let us assume that an atmospheric model simulating CO₂ concentrations can
51 represent the exact physiochemical processes but is fed with a constant CO₂ emission rate. This
52 model obviously cannot resolve the spatial distribution of CO₂ concentration because we use an
53 unresolved emission input. As another example, if we know the exact rates of CO₂ emissions but
54 use a model unable to resolve atmospheric dynamics, the spatial distribution of CO₂ concentrations
55 will be unrealistic due to unresolved physical processes.

56 Numerous scientific studies have reported on this matter. The simulations of short lifetime
57 atmospheric compounds such as nitrogen dioxide (NO₂), isoprene, formaldehyde (HCHO), and
58 the hydroxyl radical (OH) have been found to be strongly sensitive to the model spatial resolution
59 [Vinken et al., 2011; Valin et al., 2011; Yu et al., 2016; Pan et al., 2017]. Likewise, the performance
60 of weather forecast models in resolving non-hydrostatic components heavily relies on both model
61 resolution and parametrizations used. For example, when Kendon et al. [2014], Souri et al.
62 [2020a], and Wang et al. [2017] defined a higher spatial resolution in conjunction with more
63 elaborate model physics, they were able to more realistically simulate extreme or local weather
64 phenomena such as convection and sea-land breeze circulation.

65 The spatial representation issue is not only limited to models. Satellite trace gas retrievals
66 optimize the concentration of trace gases and/or atmospheric states to best match the observed
67 radiance using an optimizer along with an atmospheric radiative transfer model. This procedure
68 requires various inputs such as surface albedo, cloud and aerosol optical properties, and trace gas
69 profiles, all of which come with different scales and representation errors. Moreover, the radiative
70 transfer model by itself has different layers of complexity with regards to physics. A myriad of
71 studies have reported that satellite-derived retrievals underrepresent spatial variability whenever
72 the prognostic inputs used in the retrieval are spatially unresolved [e.g., Russell et al., 2011;
73 Laughner et al., 2018; Souri et al., 2016; Goldberg et al., 2019; Zhao et al., 2020]. Additionally,
74 the large footprint of some sensors relative to the scale of spatial variability of species inevitably
75 leads to some degree of the representativity issues [e.g., Souri et al., 2020b, Tang et al., 2021; Judd
76 et al., 2020]. It is because of this reason that several validation studies resorted to downscaling
77 their relatively coarse satellite observations using high-resolution chemical transport models so
78 that they could compare them to spatially finer datasets such as in-situ measurements [Kim et al.,
79 2018; Choi et al., 2020]. Nonetheless, their results largely arise from modeling experiments which
80 might be biased.

81 The validation of satellites or atmospheric models is widely done against pointwise
82 measurements. Mathematically, a point is an element of space. Hence, it is not meaningful to
83 associate a point with a spatial scale. If one compares a grid box to a point sample (i.e., apples to
84 oranges), they are assuming that the point is the representative of the grid box. At this point, the
85 fundamental question is: can the average of the spatial distribution of the underlying compound be
86 represented by a single value measured at a subgrid location? This question was answered in
87 Matheron [1963]. He advocated the notion of the semivariogram, a mathematical description of

88 the spatial variability, which finally led to the invention of kriging, the best unbiased linear
 89 estimator of a random field. A kriging model can estimate a geophysical quantity in a common
 90 grid. This is not exclusively special; a simple interpolation method such as the nearest neighbor
 91 has the same purpose. The power of kriging lies in the fact that it takes the data-driven spatial
 92 variability information into account and informs an error associated with the interpolated map.
 93 This strength not only makes kriging a relatively superior model over simplified interpolation
 94 methods, but also reflects the level of confidence pertaining to spatial heterogeneity dictated by
 95 both data and the semivariogram model used through its variance [Chilès and Delfiner, 2009].

96 Different studies leveraged this classical geostatistical method to map the concentrations
 97 of different atmospheric compounds at very high spatial resolutions [Tadić et al., 2017; Li et al.,
 98 2019; Zhan et al., 2018; Wu et al., 2018]; To the best of our knowledge, Swall and Foley [2009]
 99 is the only study that used kriging for a chemical transport model validation with respect to surface
 100 ozone. They suggested that kriging estimation should be executed in grids rather than discrete
 101 points. Kriging uses a semivariogram model in a continuous form. Optimizing the kriging grid size
 102 (i.e., domain discretization) at which the estimation is performed is an essence to fully obtaining
 103 the maximum spatial information from data. Another important caveat with Swall and Foley
 104 [2009] is that averaging discrete estimates (points) to build grids is not applicable for remote
 105 sensing data. Depending on the optics and the geometry, the spatial response function can
 106 transform from an ideal box (simple average) to a sophisticated shape such as a super Gaussian
 107 function (weighted average) [Sun et al., 2018]. Moreover, the footprint of satellites is not spatially
 108 constant. We will address these complications in this study using both theoretical and real-world
 109 experiments.

110 Our paper is organized with the following sections. Sections 2 is a thorough review of the
 111 concept of the semivariogram and kriging. We then provide different theoretical cases, their
 112 uncertainty, sensitivities with respect to difference tessellation, grid size, and the number of
 113 samples. Section 3 proposes a framework for satellite (model) validation using sparse point
 114 measurements and elaborates on the representation error using idealized experiments. Sections 4
 115 introduces several real-world experiments.

116 2. Semivariogram and Ordinary Kriging Estimator

117 2.1. Definition

118 The semivariogram is a mathematical representation of the degree of spatial variability (or
 119 similarity) in a function describing a regionalized geophysical quantity (f), which is defined as
 120 [Matheron, 1963]:

$$121 \gamma(\mathbf{h}) = \frac{1}{2V} \iiint_V [f(x + \mathbf{h}) - f(x)]^2 dV \quad (1)$$

122 where x is a location in the geometric fields of V , $f(x)$ is the value of a quantity at the location of x ,
 123 and \mathbf{h} is the vector of distance. If discrete samples are available rather than the continuous field,
 the general formula can be simplified to the experimental semivariogram defined as:

$$124 \gamma(\mathbf{h}) = \frac{1}{2N(\mathbf{h})} \sum_{|x_i - x_j| - |\mathbf{h}| \leq \varepsilon} [Z(x_i) - Z(x_j)]^2 \quad (2)$$

125 where $Z(x_i)$ (and $Z(x_j)$) is discrete observations (or samples), $N(\mathbf{h})$ is the number of paired
 126 observations separated by the vector of \mathbf{h} . $|\cdot|$ operator indicates the length of a vector. The condition
 127 of $|x_i - x_j| - |\mathbf{h}| \leq \varepsilon$ is to allow certain tolerance for differences in the length of the vector. For
 128 simplicity, we only focus on an isotropic case meaning we rule out the directional (or angular)
 dependency in $\gamma(\mathbf{h})$. Under this condition, the vector of \mathbf{h} becomes scalar ($h = |\mathbf{h}|$).

129 If a reasonable number of samples is present, one can describe $\gamma(h)$ through a regression
 130 model (e.g., Gaussian or spherical shapes). The degree of freedom for this regression is:

$$dof = N - p \quad (3)$$

131 where p is the number of parameters defined in the model. For instance, to fit a Gaussian function
 132 to the semivariogram with three parameters ($p=3$), three paired ($N=3$) observations are required at
 133 minimum. Different regression models can be used to describe $\gamma(h)$ depending on the
 134 characteristic of the quantity of interest. In this study, we will use a stable Gaussian function:

$$\gamma(h) = a(1 - e^{-(\frac{h}{b})^{c_0}}): c_0=1.5 \quad (4)$$

135 where a and b are fitting parameters. A non-linear least-squares algorithm based on Levenberg-
 136 Marquardt method will be used to estimate the fitting parameters.

137 The kriging estimator predicts a value of interest over a defined domain using a
 138 semivariogram model derived from samples [Chilès and Delfiner, 2009]. The kriging model is
 139 defined as [Matheron, 1963]:

$$Z(x) = Y(x) + m(x) \quad (5)$$

140 where $Y(x)$ is a zero-mean random function, and $m(x)$ is a systematic drift. If we assume
 141 $m(x) = a_0$, the model is called ordinary kriging. Similar to an interpolation problem, the
 142 estimation point (\hat{Z}), is determined by linearly combining n number of samples with their weights
 143 (λ_j):

$$\hat{Z} = \sum_{j=1}^n \lambda_j Z(x_j) + \lambda_0 \quad (6)$$

144 where \hat{Z} is the estimation, λ_0 is a constant weight, x_j is the location of samples, , and $Z(x_j)$ is point
 145 data (i.e., samples). The mean squared error of this estimation can be written as

$$E(\hat{Z} - Z_0)^2 = \text{Var}(\hat{Z} - Z_0) + \left[\lambda_0 + \left(\sum_{j=1}^n \lambda_j - 1 \right) a_0 \right]^2 \quad (7)$$

146 Where Z_0 is point observations ($Z_0 = Z(x_j), j = 1, 2, \dots, n$), and a_0 is the mean of Z which is
 147 unknown. In order to estimate the weights, we are required to minimize Eq.7, but this cannot be
 148 done without knowing the exact value of a_0 . A solution is to assume $\lambda_0 = 0$ and impose the
 149 following condition:

$$\sum_{j=1}^n \lambda_j = 1 \quad (8)$$

150 This condition warrants $E(\hat{Z} - Z_0)$ be zero and removes the need for the knowledge of a_0 .
 151 Therefore Eq.7 can be written as

$$E(\hat{Z} - Z_0)^2 = \text{Var}(\hat{Z} - Z_0) = \sum_{j_1=1}^n \sum_{j_2=1}^n \lambda_{j_1} \lambda_{j_2} \gamma_{j_1 j_2} - 2 \sum_{j_1=1}^n \lambda_{j_1} \gamma_{j_1 0} + \gamma_{00} \quad (9)$$

152 where $\gamma_{j_1 j_2}$ is the spatial covariance between the point observations and $\gamma_{j_1 0}$ is the spatial
 153 covariance of between the observations and the estimation point. The spatial covariance is modeled
 154 by a semivariogram. Using the method of Lagrange multiplier and considering the constraint on
 155 the weights, Eq.9 can be minimized by solving the following problem [Chilès and Delfiner, 2009]:

$$\begin{pmatrix} \lambda_1 \\ \vdots \\ \lambda_n \\ \mu \end{pmatrix} = \begin{pmatrix} \gamma(x_1 - x_1) \cdots \gamma(x_1 - x_n) 1 \\ \vdots \\ \gamma(x_n - x_1) \cdots \gamma(x_n - x_n) 1 \\ 1 \end{pmatrix}^{-1} \begin{pmatrix} \gamma(x_1 - x_0) \\ \vdots \\ \gamma(x_n - x_0) \\ 1 \end{pmatrix} \quad (10)$$

156 where μ is the Lagrange parameter and x_0 is the location of estimation. The first term in the right
 157 hand side of this equation shows the spatial variability described by the semivariogram model
 158 among samples, whereas the second term indicates the modeled variability between samples and
 159 the estimation point. The unknowns (the left hand side of the equation) have a unique solution if,
 160 and only if, the semivariogram model is positive definite and the samples are unique [Chilès and
 161 Delfiner, 2009]. The estimation error can be obtained by

$$\sigma^2 = E(\hat{Z} - Z_0)^2 = \sum_{j=1}^n \lambda_j \gamma_{j0} - \mu \quad (11)$$

162 This equation is an important component in the kriging estimator. Not only can we estimate $Z(x)$
 163 given a selection of data points, but also an uncertainty associated with such estimation can be
 164 provided.

165 2.2. Theoretical Cases

166 2.2.1. Sensitivity to spatial variability of the field

167 The present section illustrates the application of ordinary kriging for several numerical
 168 cases. Five idealized cases are simulated in a grid of 100×100 pixels, namely, a constant field (C1),
 169 a ramp starting from zero in the lower left to higher values in the upper right (C2), an intersection
 170 with concentrated values in four corridors (C3), a Gaussian plume placed in the center (C4), and
 171 multiple Gaussian plumes spread over the entire domain (C5). We randomly sample 200 data
 172 points from each field as is, and successively create the semivariograms in 100 binned distances.
 173 Except C1, which lacks a spatial variability thus $\gamma(h) = 0$, other semivariograms are fit with the
 174 stable Gaussian function. Using the semivariogram model, we optimize Eq.10 to estimate $\hat{Z}(x)$
 175 for each pixel (i.e., 100×100) with the estimation errors based on Eq.11. Figure 1 depicts the truth
 176 field ($Z(x)$), semivariograms made from the samples, estimated values ($\hat{Z}(x)$), difference of $Z(x)$
 177 and $\hat{Z}(x)$, and error associated with the estimation.

178 As for C1, the uniformity results in a constant semivariogram leading the estimation to be
 179 identical to the truth. This estimation signifies the unbiased characteristic of ordinary kriging. C1
 180 is never met in reality, however, it is possible to assume some degree of uniformity among data
 181 restrained to background values; a typical example of this can be seen in the spatial distribution of
 182 a number of trace gases in pristine environments such as NO_2 [e.g., Wang et al., 2020] and HCHO
 183 [Wolfe et al., 2019]. Under this condition, any data point within the field (i.e., the satellite
 184 footprint) can be assumed to be representative of the spatial variability in truth.

185 Concerning C2, the semivariogram shows a linear shape meaning data points at larger
 186 distances exhibit larger differences. Generally geophysical samples are uncorrelated at large
 187 distances, thereby one expects the semivariogram to increase more slowly as the distance gets
 188 further. The steady increase in $\gamma(h)$ is indicative of a systematic drift in the data invalidating the
 189 assumption of $m(x) = a_0$. In many applications, a simple polynomial can explain $m(x)$ and
 190 subsequently be subtracted from the data points. An example of this problem is tackled by Onn
 191 and Zebker [2006]; it concerns the spatial variability of water vapor columns measured by GPS
 192 signals. Onn and Zebker [2006] observed a strong relationship between the water vapor columns
 193 and GPS altitudes resulting from the vertical distribution of water vapor in the atmosphere.
 194 Because of this complication, a physical drift model describing the vertical dependency was fit

195 and removed from the measurements so that they could focus on the horizontal fluctuations. In
196 terms of C2, one can effortlessly reproduce $Z(x)$ by fitting a three-dimensional plane to barely
197 three samples, indicating that the semivariogram is of little use.

198 C3 is an example of an extremely inhomogeneous field manifested in the stabilized
199 semivariogram at a value of $\gamma \sim 500$, called the sill [Chilès and Delfiner, 2009], indicating
200 insignificant information (variance) from the samples beyond this distance (~ 20), called the range.
201 Range is defined as the separation distance at which the total variance in data is extracted. The
202 smaller the range is, the more heterogeneous the samples will be. While the estimated field roughly
203 captures the shape of the intersections, it is spatially distorted at places with relatively sparse data
204 points. The kriging model error is essentially a measure of the density of information. It converges
205 to zero in the samples location and diverges to large values in gaps.

206 C4 is a close example of a point source emitter with faint winds and turbulence. The
207 semivariogram exhibits a bell shape. As samples get further from the source, the variance diverges,
208 stabilizes, and then sharply decreases. This is essentially because many data points with low
209 values, apart from each other, have negligible differences. This tendency is recognized as the hole
210 effect which is characterized for high values to be systemically surrounded by low values (and
211 vice versa). It is possible to mask this effect by fitting a semivariogram model stabilizing at certain
212 sill (like the one in Figure 1). Nonetheless, if the semivariogram shows periodic holes, the fitted
213 model should be modified to a periodic cosine model [Pyrcz and Deutsch, 2003].

214 The last case, C5, shows a less severe case of the hole effect previously observed in C4.
215 This is due to the presence of more structured patterns in different parts of the domain. The range
216 is roughly twice as large as the previous case (C4) denoting that there is more information
217 (variance) among the samples at larger distances. A number of experiments using this particular
218 case will be discussed in the following subsections.

219 *2.2.2. Sensitivity to the number of samples*

220 It is often essential to optimize the number of samples used for kriging. The kriging
221 estimator somewhat recognizes its own capability at capturing the spatial variability through
222 Eq.11. Thus, if the target is spatially too complex and/or the samples are too limited, the estimator
223 essentially informs that $\hat{Z}(x_0)$ is unreliable through large variance. However, there is a caveat;
224 $Y(x)$ must be a Gaussian random model with a zero mean so that kriging can capture the statistical
225 distribution of \hat{Z} given the data points. Except this case, the kriging variance can either be
226 underestimated or overestimated depending on the level of skewness of the statistical distribution
227 of $Y(x)$ [Armstrong, 1994]. Figure 2 shows the kriging estimation for C5 using 5, 25, 50, 100, and
228 500 random samples in the entire field. Immediately apparent is a better description of the
229 semivariogram when larger number of samples are used, which in turn, results in a better
230 estimation of $Z(x)$. The optimum number of samples to reproduce $Z(x)$ depends on the
231 requirement for the relative error ($\sigma/Z(x)$) being met at a given location.

232 *2.2.3. Sensitivity to the tessellation of samples*

233 A common application of kriging is to optimize the tessellation of data points for a fixed
234 number of samples to achieve a desired precision. In real-world practices, the objective of such
235 optimization is very purpose-specific, for example, one might prefer a spatial model representing
236 a certain plume in the entire domain. Different ways for data selection exist [e.g., Rennen, 2008],
237 but for simplicity, we focus on four categories: purely random, stratified random, a uniform grid,
238 and an optimized tessellation. Figure 3 demonstrates the estimation of C5 using 25 samples chosen
239 based on those four procedures.

Concerning the random selection, the lack of samples over two minor plumes cause the estimation to deviate largely from the truth. While a random selection may seem to be practical because it is independent of the underlying spatial variability, it can suffer from under sampling issues, thus being inefficient. As a remedy, it might be advantageous to group the domain into similar zones and randomly sample from each, which is commonly known as stratified random selection. We classify the domain into four zones by running the k-mean algorithm on the magnitudes of $Z(x)$ (not shown) and randomly sample six to seven points from each one (total 25). We achieve a better agreement between the estimated field and the truth because we exploited some prior knowledge (here the contrast between low and high values).

As for the uniform grid, we notice that there are fewer data points in the semivariogram stemming from redundant distances which is indicative of correlated information. Nonetheless, if the desired tessellation is neutral with regard to location meaning that all parts of the domain is equal of scientific interest, the uniform grid is the most optimal design for the prediction of $Z(x)$ under an ideally isotropic case. A mathematical proof for this claim can be found in Chilès and Delfiner [2009].

To execute the last experiment, we select 25 random samples for 1000 times and find the optimal estimation by finding the minimum sum of $|\hat{Z}(x_0) - Z(x)|$. It is worth mentioning that the optimized tessellation is essentially a local minimum based on 1000 kriging attempts. The optimized location of samples seems to more clustered over areas with large spatial gradients. Not too surprisingly, we observe the smallest discrepancy between the estimation and the truth.

A lingering concern over the application of these numerical experiments is that the truth is assumed to be known. The truth is never known, by this means we may never exactly know how well or poorly the kriging estimator is performing. However, it is highly unlikely for some prior understandings or expectations of the truth to be absent. If this is the case, which is rare, a uniform grid should be intuitively preferred to deliver the local estimations of average values in uniform blocks. In contrast, if the prior knowledge is articulated by previous site visits, model predictions, theoretical experiments, pseudo-observations, or other relevant data, the tessellation needs to be optimized.

It is important to recognize that the uncertainties associated with the prior knowledge directly affects the level of confidence in the final answer. Accordingly, the prior knowledge error should ultimately be propagated to the kriging variance. The determination of the prior error is often done pragmatically. For example, if the goal is to design the location of thermometer sites to capture surface temperature during heat waves using a yearly averaged map of surface temperature, it would be wise to specify a large error with this specific prior information to play down the proposed design. This is primarily because the averaged map underrepresents such an atypical case. A possible extension of this example would be to use a weather forecast model with quantified errors capable of capturing retrospective heat waves. Although a reasonable forecast in the past does not necessarily guarantee a reasonable one in the future, it is rational to assume for the uncertainty with a new tessellation design using the weather model forecast to be lower than that of using the averaged map.

A general roadmap for the data tessellation design is shown in Figure 4. As proven in Chilès and Delfiner [2009], if the field is purely isotropic, the uniform grid is the most intuitive sensible choice when the prior information on the spatial variability is lacking. When the prior knowledge with quantified errors is available, an optimum tessellation can be achieved by running a large number of kriging models with suitable $\gamma(h)$ and picking the one yielding the minimum difference between the prior knowledge and the estimation. The choice of the cost function (here L1 norm)

286 is purpose-specific. For example, if the reconstruction of a major plume was the goal, using a
287 weighted cost function, geared towards capturing the shape of plume, would be more appropriate.

288 2.2.4. *Sensitivity to the grid size*

289 A kriging model can estimate a geophysical quantity at a desired location considering the
290 data-driven spatial variability information. Since the kriging model is practically in a continuous
291 form, the desired locations can be anywhere within the field of V . A question is whether or not it
292 is necessary to map the data onto a very fine grid. There is a trade-off between the computational
293 cost and the accuracy of the interpolated map. The range of the underlying semivariogram helps
294 in finding the optimal solution. The greater the range (i.e., a more homogeneous field), the less
295 important to map the data in a finer grid.

296 Figure 5a depicts an experiment comparing the estimates of C2 at different grid sizes with
297 the truth. The departure of the estimate from the truth is rather negligible for several coarse grids
298 (e.g., 10×10). The homogeneous field, manifested by the large range (Figure 1), allows for a
299 reasonable estimation of $Z(x)$ at coarse resolutions with inexpensive computational costs. Figure
300 5b shows the same experiment but on C5 with the optimized tessellation. As opposed to the
301 previous experiment, the estimate substantially diverges from the truth when increasing the grid
302 size, suggesting that a finer resolution should be used for fields with smaller ranges (i.e.,
303 heterogeneous fields).

304 The complexity of directly using the range for choosing the optimal grid size arises from
305 the fact that the level of spatial homogeneity can vary within the domain. In fact, the range is
306 derived from a semivariogram model representing a crude estimate of varying ranges occurring at
307 various scales. It is intuitively clear that depending on the degree of heterogeneity, which is
308 spatiotemporally variable, the grid size needs to be adaptively adjusted [Bryan, 1999]. For the sake
309 of simplicity, but at a higher computational cost, we adopt a numerical solution which is to first
310 simulate on a coarse grid, then on a finer one until the difference with respect to the previous grid
311 size across all pixels reaches to an acceptable value (<1%). We name this output (1×1) with the
312 optimized tessellation for C5 as C5opt.

313 3. Comparison of points to satellite pixels

314 3.1. *Synching the scales between the gridded field and satellite pixels*

315 To minimize the complications of different spatial scales between two gridded data, we
316 first need to upscale the finer resolution data to match the coarse ones. In case of numerical
317 chemical transport or weather forecast models, the size of the grid box is definitive. Likewise, a
318 satellite footprint, mainly dictated by the sensor design, the geometry, and signal-to-noise
319 requirements [Platt et al., 2021], is known. However, the grid size of the kriging estimation is a
320 variable subject to optimization which has been discussed previously.

321 When we compare the grid size of the kriging estimate to that of a satellite (or a model),
322 three situations arise: First, the kriging spatial resolution is coarser than the satellite, a condition
323 occurring when either the field is homogeneous or the field is under sampled. In situations where
324 the field is homogeneous ($\gamma(h) \approx 0$), it is safe to directly compare the data points to the satellite
325 measurements without having to use kriging. If the under sampling is the case (see Figure 2 with
326 5 samples), it is sensible to first investigate if the field is homogeneous within the satellite footprint
327 using different data (if any). If the homogeneity is met, we either can compare two datasets without
328 kriging or to match the size of kriging grid cell with the satellite footprint and statistically involve
329 the kriging variance in the comparison (discussed later); nonetheless, the kriging estimate beyond
330 the location of samples must be used with extra caution because their variance very quickly
331 departures from zero to extremely large numbers (see Figure 1). Thus, there is a compromise

332 between increasing the number of paired samples between two datasets and enhancing the level of
 333 confidence in statistics. If independent observations suggest that there might be large heterogeneity
 334 within a satellite footprint, it is strongly advised against quantitatively comparing the points to the
 335 satellite observations. Second, the number of samples is fewer than three observations in the field
 336 so it is in principal impossible to build a semivariogram. Validating a satellite under this condition
 337 is prone to misinterpretation because the spatial heterogeneity cannot be modeled. Nonetheless, if
 338 one presumes a good degree of homogeneity within the sensor footprint (such as very high-
 339 resolution remote sensing airborne data), the direct comparison of point measurements might be
 340 possible. Third, the satellite footprint is coarser than the kriging estimate. Under this condition, we
 341 upscale the kriging map to match the spatial resolution of the satellite using

$$\hat{Z}_c = \hat{Z}_f * S = \int \hat{Z}_f(x) S(x - y) dy \quad (12)$$

342 where S is the spatial response function, \hat{Z}_c is the coarse kriging field, $\langle * \rangle$ is the convolution
 343 operator, y is shift, and \hat{Z}_f is the fine field. In discrete form we can rewrite Eq.12 in

$$\hat{Z}_c[i, j] = \sum_m \sum_n \hat{Z}_f[i - m, j - n] S[m, n] \quad (13)$$

344 where m and n are the dimension of the response function. The mathematical formulation of
 345 $S[m, n]$ for a number of satellites can be represented by two-dimensional super Gaussian functions
 346 as discussed in Sun et al. [2018]. Atmospheric models have a uniform response to the simulated
 347 values within a grid box, therefore $S[m, n] = \frac{1}{m \times n} J_{m, n}$, where J is the matrix of ones. In the same
 348 way, the kriging variance should be convolved through

$$\sigma_c^2[i, j] = \sum_m \sum_n \sigma_f^2[i - m, j - n] S^2[m, n] \quad (14)$$

349 where a superscript of 2 denotes squaring, and σ_c^2 and σ_f^2 are the kriging variance in the coarse
 350 and the fine grids, respectively.

351 To demonstrate the upscaling procedure, we use C5opt (1×1) and upscale it at six grid sizes
 352 (m, m) of 5×5 , 10×10 , 15×15 , 20×20 , 25×25 , and 30×30 . For simplicity, we consider $S = \frac{1}{m^2} J_{m, m}$;
 353 this spatial response function results in averaging the values in the grid boxes. Figure 6 shows the
 354 resultant map overplotted with the samples along with the error estimation. Two tendencies from
 355 this experiment can be identified: First, the discrepancy of the point data and \hat{Z} is becoming more
 356 noticeable as the grid size grows; this directly speaks to the notion of the spatial representativeness;
 357 large grid boxes are less representative of sub-grid values. Second, the gradients of the field along
 358 with the estimation error become smoother primarily due to convolving the field with the spatial
 359 response function, which acts as a low pass filter.

360 We further directly compare \hat{Z} to the samples (i.e., observations) shown in Figure 7. We
 361 see an excellent comparison between \hat{Z} at 1×1 resolution with the observations underscoring the
 362 unbiasedness characteristic of the kriging estimator. Conversely, the upscaled field gradually
 363 diverges from the observations. This divergence is *the problem of scale*.

364 **3.2. Point to pixel vs pixel to pixel**

365 To elaborate on the problem of scale, we design an idealized experiment theoretically
 366 validating pseudo satellite observations against some pseudo point measurements. The pseudo
 367 satellite observations are created by upscaling the C5 truth (Z) to 30×30 grid footprint considering

368 $S = \frac{1}{m^2} J_{m,m}$, meaning that the satellite is observing the truth but in a different scale (Figure S1).
 369 The pseudo point measurements are the ones used for C5opt. Figure 8a shows the direct
 370 comparison of the satellite pixel with the point observations. By ignoring the fundamental fact that
 371 these two datasets are inherently different in nature, displaying the same geophysical quantity by
 372 at different scales, we observe a perceived discrepancy ($r^2=0.64$). The comparison suggests a
 373 wrong conclusion that the satellite observations are biased-low. This discrepancy is unrelated to
 374 any observational or physical errors, rendering any physical interpretation of the comparison
 375 biased due to spatial-scale differences in the data sets. Figure 8b depicts the comparison of each
 376 grid box of the upscaled kriging estimate (30×30) with that of the satellite. This direct comparison
 377 shows a strong degree of agreement ($r^2=0.98$), shaking off the erroneous idea of directly comparing
 378 point to gridded data when the field exhibits substantial spatial heterogeneity.

379 Yet, the comparison misses an important point: the kriging estimate is considered error-
 380 free. We attempt to incorporate the kriging variance through a Monte Carlo linear regression
 381 method. Here, the goal is to find an optimal linear fit ($y = ax + b + \varepsilon$) such that $\chi^2 =$
 382 $\sum \frac{[y - f(x_i, a, b)]^2}{\sigma_y^2 + a^2 \sigma_x^2}$ is minimized. σ_y^2 and σ_x^2 are the variances of y (here the satellite) and x (the kriging
 383 variance), respectively. We set the errors of y to zero, and randomly perturb the errors of x based
 384 on a normal distribution with zero mean and a standard deviation equal to that of kriging estimate
 385 15,000 times. The average of optimized a and b coefficients derived from each fit are then
 386 estimated and their deviation at 95% confidence interval assuming a Gaussian distribution is
 387 determined. Figure 8b,c show the linear fit with and without considering the kriging error estimate.
 388 The linear fit without involving the kriging error gives a strong impression that it is nearly perfect,
 389 following closely to the paired observations. This is essentially explainable by the primary goal of
 390 χ^2 which is to minimize the L2 norm of residuals ($y - f(x_i, a, b)$), portraying a very optimistic
 391 picture of the satellite validation. The linear fit considering the kriging errors is different. The
 392 uncertainties associated with a and b are larger since x is variable (shown in horizontal error bars).
 393 The optimal fit gravitates towards the points with smaller standard deviations as they impose a
 394 larger weight. The confidence in the linear fit at higher values is lower due to their errors being
 395 large. This fit is a more realistic portrayal of the satellite validation.

396 Figure 9 summarizes the general roadmap for satellite (and model) validations against point
 397 measurements. To fit the semivariogram with at least two parameters, we are required to have
 398 three samples at minimum. Therefore, it is implausible to derive the spatial information from the
 399 point data where sampling is extremely sparse (<3 samples within the field). The only case of
 400 directly comparing point and satellite pixels is when the field within satellite footprint or the field
 401 in general is rather homogeneous confirmed by independent data/models. Having more samples
 402 allows to acquire some information on the spatial heterogeneity. The information carried by the
 403 data is considered more and more robust with increasing the number of samples. Subsequently,
 404 the kriging map along with its variance derived from a reasonable semivariogram at an optimized
 405 grid resolution should be convolved with the satellite response function so that we can conduct an
 406 apples-to-apples comparison. A real-world example on the satellite validation will be shown later.

407 4. Real-world experiments

408 4.1. Spatial distribution of NO₂

409 We begin with focusing on tropospheric NO₂ columns observed by TROPOMI sensor
 410 [Copernicus Sentinel data processed by ESA and Koninklijk Nederlands Meteorologisch Instituut
 411 (KNMI), 2019; Boersma et al., 2018] at ~13:30 LST. We choose NO₂ primarily due to its spatial
 412 heterogeneity [e.g., Souri et al., 2018; Nowlan et al., 2016, 2018; Valin et al., 2011; Judd et al.,

413 2020]. We oversample good quality pixels ($qa_flag > 0.75$) through a physical-based gridding
414 approach [Sun et al., 2018] over Texas at $3 \times 3 \text{ km}^2$ resolution in four seasons in 2019. We extract
415 samples by uniformly selecting the NO_2 columns in the center of each $30 \times 30 \text{ km}^2$ block. The
416 semivariogram along with its model are calculated, and then we krig the samples. Figure 10 shows
417 the NO_2 columns map for four different seasons, the semivariogram, the kriging estimates, and the
418 differences between the estimate and the field. High levels of NO_2 are confined to cities indicating
419 the sources being predominantly anthropogenic. Wintertime NO_2 columns are larger than
420 summertime mainly due to meteorological conditions and the OH cycle, the major sink of NO_2 .
421 All semivariograms exhibit the hole effect. This is because of high values of NO_2 being
422 systematically surrounded by low values. Regardless of the season, we fit the stable Gaussian to
423 variances at distances smaller than 2.5° ($\sim 275 \text{ km}^2$). The b_0 parameter explaining the length scale
424 is found to be 0.94, 0.88, 0.71, and 0.83 degree for DJF, MAM, JJA, and SON, respectively. These
425 numbers strongly coincide with the seasonal lifetime of NO_2 [Shah et al., 2020]; wintertime NO_2
426 columns are spatially more uniform around the sources thus in relative sense, they are more
427 homogeneous (spatially correlated) than those in warmer seasons. On the other hand, the shorter
428 NO_x lifetime in summer results in a steeper gradient of NO_2 concentrations. This tendency should
429 not be generalized because transport and various NO_x sources including biomass burning, soil
430 emissions, and lightning and can have large spatiotemporal variability resulting in different length
431 scales in different times of a year. The differences between the kriging estimate and the field show
432 some spatial structures indicating that NO_2 is greatly heterogenous.

433 **4.2. Optimized tessellation over Houston**

434 The preceding TROPOMI data enabled us to optimize a tessellation of ground-based point
435 spectrometers over Houston. Our goal here is to propose an optimized network for winter 2021
436 given our knowledge on the spatial distribution of NO_2 columns in winter 2019 measured by
437 TROPOMI. The assumption of using a retrospective NO_2 field for informing a hypothetical future
438 campaign is not entirely unrealistic. If we have a consistent number of pixels from TROPOMI
439 between two years, it is unlikely for the spatial variance of NO_2 to be substantially different for
440 the same season. We follow the framework proposed in Sect. 2.2.3 involving randomly selecting
441 samples from the field (for 50000 iteration), and calculating kriging estimates for a given number
442 of spectrometers. We then chose the optimum tessellation based on the minimum sum of $|\hat{Z}(x_0) -$
443 $Z(x)|$.

444 Figure 11 shows the optimized tessellation given 5, 10, 15, and 20 spectrometers over
445 Houston. The Houston plume is better represented with more samples being used. All cases share
446 the same feature; the optimized samples are clustered in the proximity or within the plume. This
447 tendency is clearly intuitive. We are required to place the spectrometers in locations where a
448 substantial gradient (variance) in the field is expected. The difference between kriging estimate
449 and the TROPOMI observations using 20 samples does not substantially differ in comparison to
450 the one using 15 samples. Therefore, to keep the cost low, a preferable strategy is to keep the
451 number of spectrometers as low as possible while achieving a reasonable accuracy. Based on the
452 presented results, the optimized tessellation using 15 samples is preferred among others because it
453 achieves roughly the same accuracy as the one with 20 samples.

454 **4.3. Validating OMI tropospheric NO_2 columns during DISCOVER-AQ 2013 campaign using 455 Pandora**

456 In order to understand ozone pollution [e.g., Mazzuca et al., 2016; Pan et al., 2017; Pan et
457 al., 2015], characterize anthropogenic emissions [Souri et al., 2016, 2018], and validate satellite
458 data [Choi et al., 2020], an intensive air quality campaign was made in September 2013 over

459 Houston (DISCOVER-AQ). The campaign encompassed a large suite of Pandora spectrometer
 460 instrument (PSI) (11 stations) measuring total NO_2 columns with a high precision (2.7×10^{14}
 461 molecules cm^{-2}) and a moderate nominal accuracy (2.7×10^{15} molecules cm^{-2}) under the clear-sky
 462 condition [Herman et al., 2009]. We remove the observations with an error of >0.05 DU,
 463 contaminated by clouds, and averaged them over the month of September at 13:30 LST (± 30
 464 mins). We attempt to validate OMI tropospheric NO_2 columns version 3.0 [Bucsela et al., 2013]
 465 refined in Souri et al. [2016] with the 4-km model profiles. The OMI sensor resolution varies from
 466 $13 \times 34 \text{ km}^2$ at nadir to $\sim 40 \times 160 \text{ km}^2$ at the edge of the scan line. Biased pixels were removed based
 467 on cloud fraction > 0.2 , terrain reflectivity > 0.3 , and main (xtrack) quality flags =0. Following
 468 Sun et al. [2018], we oversample high quality pixels in the month of September 2013 over Houston
 469 at $0.2 \times 0.2^\circ$ resolution. To remove the stratospheric contributions from PSI measurements, we
 470 subtract OMI stratospheric NO_2 ($2.8 \pm 0.16 \times 10^{15}$ molecules cm^{-2}) from the total columns over the
 471 area. Figure 12 shows the monthly-averaged tropospheric NO_2 columns measured by OMI
 472 overplotted by 11 PSIs. The elevated NO_2 levels (up to $\sim 6 \times 10^{15}$ molecules cm^{-2}) are seen over the
 473 center of Houston.

474 We then follow the validation framework shown in Figure 9 in which the number of point
 475 measurements and the level of heterogeneity are the main factors in deciding if we should directly
 476 compare them to the satellite pixels. Figure 13 shows the monthly-averaged PSI measurements
 477 along with the semivariogram and resulting kriging estimate at an optimized resolution ($\sim 2 \text{ km}^2 =$
 478 13800 data over the entire region) and errors. The distribution of semivariogram suggests that there
 479 is a strong degree of spatial heterogeneity, necessitating the use of kriging. We fit a stable Gaussian
 480 to the semivariogram resulting in $2.23 \times (1 - e^{-(\frac{h}{0.19})^{1.5}})$. The spatial information (variance) levels
 481 off at 0.19° ($\sim 21 \text{ km}$) with a maximum variance equal to $2.23 \text{ molecules}^2 \text{ cm}^{-4}$. The measurements
 482 beyond this range (21 km) have a minimal weight due to this length scale. It is because of this
 483 reason that we see the kriging estimate converges to a fixed value at places being further than this
 484 range. The kriging errors of those grid boxes are constantly large (40% relative error). The
 485 optimum grid size for kriging is found to be 2 km^2 ($< 1\%$ difference across all grid boxes).
 486 Subsequently, we use the super Gaussian spatial response function described in Sun et al. [2018]
 487 to convolve both the kriging estimate and error within (see Figure S2). Figure 14 shows the
 488 differences between the kriging estimate and error before and after convolution. The response
 489 function (OMI pixel) tends to be on average coarser than 2 km^2 resulting in smoothing of both the
 490 kriging estimate and error.

491 We ultimately conduct two different sets of comparison: directly comparing PSI to OMI
 492 pixels, and comparing convolved kriged PSI to OMI. It is worth noting that PSI measurements are
 493 monthly-averaged; similarly OMI data are oversampled in a monthly basis. In terms of the PSI,
 494 we only account for grid boxes whose kriging error is below 1.2×10^{15} molecules cm^{-2} (1193
 495 samples, 8% of total kriging grid boxes). As for the grid-to-grid comparison, the kriging variance
 496 is considered in the linear polynomial fitted to the data through the Monte Carlo of chi-square with
 497 5,000 iterations. The variability with the OMI stratospheric NO_2 columns (0.16×10^{15} molecules
 498 cm^{-2}) is added to the PSI error for both analyses. The left and right panels of Figure 15 show the
 499 comparisons. As for the direct comparison of actual points (PSI) to pixels (OMI), the PSI
 500 measurements indicate a deviation of the slope ($r^2=0.66$) from the unity line. This suggests that
 501 there is an unresolved magnitude-dependent systematic error. The grid-to-grid comparison not
 502 only offers a clearer picture of the distribution of data points, but also it hints at the offset being
 503 rather constant ($0.66 \pm 0.18 \times 10^{15}$ molecules cm^{-2} ; $r^2=0.72$). We also observe that the statistics
 504 between the satellite and the benchmark are moderately improved. This comparison in general

505 provides an important implication: the varying offsets in a plume shape environment (high to low
506 values) are not necessarily due to variable offsets in the satellite retrieval, as the kriging estimate
507 suggests that those varying offsets in point-to-pixel comparison, manifested in slope = 0.76, are a
508 result of varying spatial scales.

509 **Summary**

510 There needs to be increased attention to the spatial representativity in the validation of
511 satellite (model) against pointwise measurements. A point is the element of space, whereas satellite
512 (model) pixels (grid box) are (at best) the product of the integration of infinitesimal points and a
513 normalized spatial response function. If the spatial response function is assumed to be an ideal
514 box, the resulting grid box will represent the average. Essentially, no justifiable theory exists to
515 accept that the averaged value of a population should absolutely match with a sample, unless all
516 samples are identical (i.e., a spatially homogeneous field). This glaring fact is often overlooked in
517 the atmospheric science community. At a conceptual level, we are required to translate pointwise
518 data to the grid format (i.e., rasterization). This can be done by modeling the spatial autocorrelation
519 (or semivariogram) extracted from the spatial variance (information) among measured sample
520 points. Assuming that the underlying field is a random function with an unknown mean, the best
521 linear unbiased predictions of the field can be achieved by kriging using the modeled
522 semivariograms.

523 In this study, we discussed methods for the kriging estimation of several idealized cases.
524 Several key tendencies were observed through this experiment: first, the range corresponded to the
525 degree of spatial heterogeneity; a larger range indicated the less presence of heterogeneity. Second,
526 the kriging variance explaining the density of information quickly diverged from zero to large
527 values when the field exhibited large spatial heterogeneity. This tendency mandates increasing the
528 number of samples (observations) for those cases. Third, while the semivariogram models were
529 constructed from discrete pair of samples, they are mathematically in a continuous form. It is
530 because of this reason that we determined the optimal spatial resolution of the kriging estimate by
531 incrementally making the grids finer and finer until a desired precision (=1%) was met.

532 The present study applied kriging to achieve an optimum tessellation given a certain
533 number of samples such that the difference between our prior knowledge of the field, articulated
534 by previous observations, models or theory, and the estimation is minimal. Usually there is
535 uncertainty about the prior knowledge that should be propagated to the final estimates. The
536 optimum tessellation for a range of idealized and real-world data consistently voted for placing
537 more samples in areas where the gradients in the measurements were significant such as those
538 close to point emitters.

539 This study also revisited the spatial representativity issue; it limits the realistic
540 determination of biases associated with satellites (models). In one experiment, we convolved the
541 kriging estimate for a multi-plume field with a box filter but various sizes. The perfect agreement
542 ($r=1.0$) between the samples (point) and kriging output (pixel) seen at a high spatial resolution
543 gradually vanished with coarsening of the resolution of grid boxes ($r=0.8$). We also directly
544 compared samples (point) with pseudo satellite observations (showing the truth) with a coarse
545 spatial resolution which led to a flawed conclusion about the satellite being biased-low. We
546 modeled the semivariogram of those samples, estimated the field using kriging, and convolved
547 with the pseudo-satellite spatial response function. The direct comparison of this output with that
548 of the satellite showed a completely different story suggesting that the data were rather free of any
549 bias. A serious caveat with using a spatial model (here kriging) is that it consists of errors: the
550 estimations being further from samples are less certain. It is widely known that discounting the

551 measurement/model errors in true straight-line relationship between data can introduce artifacts.
552 To consider the kriging variance in the comparisons we employed a Monte Carlo method on chi-
553 square optimization which ultimately allowed us to not only provide a set of solutions within the
554 range of the uncertainty of the kriging model, but also to assign smaller weights on gross estimates.

555 We further validated monthly-averaged Ozone Monitoring Instrument (OMI) tropospheric
556 NO₂ columns using 11 Pandora Spectrometer Instrument (PSI) observations over Houston during
557 NASA's DISCOVER-AQ campaign. A pixel-to-point comparison between two dataset suggested
558 varying biases in OMI manifested in a slope far from the identity line. By contrast, the kriging
559 estimate from the PSI measurements, convolved with the OMI spatial response function, resulted
560 in an inter-comparison slope close to the unity line. This suggested that there was only a constant
561 systematic bias ($0.66 \pm 0.18 \times 10^{15}$ molecules cm⁻²) associated with the OMI observations which
562 does not vary with tropospheric NO₂ column magnitudes.

563 The central tenants of satellite and model validation are pointwise measurements. Our
564 experiments paved the way for a clear roadmap explaining how to transform these pointwise
565 datasets to a comparable spatial scale relative to satellite (model) footprints. It is no longer
566 necessary to ignore *the problem of scale*. The validation against point measurements can be
567 carefully conducted in the following steps:

- 569 i. Construct the experimental semivariogram if the number of point measurements
570 allows (usually ≥ 3 within the field; the field can vary depending on the length
571 scale of the compound).
- 572 ii. Drop the quantitative assessment if the number of point measurements are
573 insufficient to gain spatial variance and the prior knowledge suggests a high
574 likelihood of spatial heterogeneity within the field.
- 575 iii. Choose an appropriate function to model the semivariogram.
- 576 iv. Estimate the field with kriging (or any other spatial estimator capable of digesting
577 the semivariogram) and calculate the variance.
- 578 v. Estimate the optimum grid resolution of the estimate.
- 579 vi. Convolve the kriging estimate and its variance with the satellite (model) spatial
580 response function (which is sensor specific).
- 581 vii. Conduct the direct comparison of the convolved kriged output and the satellite
582 (model) considering their errors through a Monte Carlo (or a weighted least-squares
583 method).

584
585 Recent advances in satellite trace gas retrievals and atmospheric models have helped
586 extend our understanding of atmospheric chemistry but an important task before us in improving
587 our knowledge on atmospheric composition is to embrace the semivariogram (or spatial auto-
588 correlation) notion when it comes to validating satellites/models using pointwise measurements,
589 so that we can have more robust quantitative applications of the data and models.

590 Acknowledgement

591 Amir Souri and Matthew Johnson were funded for this work through NASA's Aura Science Team
592 (grant number: 80NSSC21K1333). Kang Sun acknowledges support by NASA's Atmospheric
593 Composition: Modeling and Analysis (ACMAP) program (grant number: 80NSSC19K09). We
594 thank many scientists whose concerns motivated us to tackle the presented problem. In particular,
595 we thank Chris Chan Miller, Ron Cohen, Jeffrey Geddes, Gonzalo González Abad, Christian
596 Hogrefe, Lukas Valin, and Huiqun (Helen) Wang.

597 **Author contributions**
598 AHS designed the research, executed the experiments, analyzed the data, made all figures, and
599 wrote the paper. KS implemented the oversampling method, provided the spatial response
600 functions, and oversampled TROPOMI data. KC, XL, and MSJ helped with the conceptualization
601 of the study and the interpretation of the results. All authors contributed to discussions and edited
602 the paper.
603

604 **References**
605

606 Armstrong, M.: Is Research in Mining Geostats as Dead as a Dodo?, in: Geostatistics for the
607 Next Century: An International Forum in Honour of Michel David's Contribution to
608 Geostatistics, Montreal, 1993, edited by: Dimitrakopoulos, R., Springer Netherlands,
609 Dordrecht, 303–312, https://doi.org/10.1007/978-94-011-0824-9_34, 1994.

610 Boersma, K. F., Eskes, H. J., Richter, A., De Smedt, I., Lorente, A., Beirle, S., van Geffen, J. H.
611 G. M., Zara, M., Peters, E., Van Roozendael, M., Wagner, T., Maasakkers, J. D., van der
612 A, R. J., Nightingale, J., De Rudder, A., Irie, H., Pinardi, G., Lambert, J.-C., and
613 Compernolle, S. C.: Improving algorithms and uncertainty estimates for satellite NO₂
614 retrievals: results from the quality assurance for the essential climate variables
615 (QA4ECV) project, *Atmos. Meas. Tech.*, 11, 6651–6678, <https://doi.org/10.5194/amt-11-6651-2018>, 2018.

617 Bryan, G. L.: Fluids in the universe: adaptive mesh refinement in cosmology, *Comput. Sci. Eng.*,
618 1, 46–53, <https://doi.org/10.1109/5992.753046>, 1999.

619 Bucsela, E. J., Krotkov, N. A., Celarier, E. A., Lamsal, L. N., Swartz, W. H., Bhartia, P. K.,
620 Boersma, K. F., Veefkind, J. P., Gleason, J. F., and Pickering, K. E.: A new stratospheric
621 and tropospheric NO₂ retrieval algorithm for nadir-viewing satellite instruments:
622 applications to OMI, *Atmos. Meas. Tech.*, 6, 2607–2626, <https://doi.org/10.5194/amt-6-2607-2013>, 2013.

624 Chilès, J.-P. and Delfiner, P.: *Geostatistics: Modeling Spatial Uncertainty*, John Wiley & Sons,
625 718 pp., 2009.

626 Choi, S., Lamsal, L. N., Follette-Cook, M., Joiner, J., Krotkov, N. A., Swartz, W. H., Pickering,
627 K. E., Loughner, C. P., Appel, W., Pfister, G., Saide, P. E., Cohen, R. C., Weinheimer, A.
628 J., and Herman, J. R.: Assessment of NO₂ observations during DISCOVER-AQ and
629 KORUS-AQ field campaigns, *Atmos. Meas. Tech.*, 13, 2523–2546,
630 <https://doi.org/10.5194/amt-13-2523-2020>, 2020.

631 Goldberg, D. L., Saide, P. E., Lamsal, L. N., de Foy, B., Lu, Z., Woo, J.-H., Kim, Y., Kim, J.,
632 Gao, M., Carmichael, G., and Streets, D. G.: A top-down assessment using OMI NO₂
633 suggests an underestimate in the NO_x emissions inventory in Seoul, South Korea, during
634 KORUS-AQ, *Atmos. Chem. Phys.*, 19, 1801–1818, <https://doi.org/10.5194/acp-19-1801-2019>, 2019.

636 Herman, J., Cede, A., Spinei, E., Mount, G., Tzortziou, M., and Abuhassan, N.: NO₂ column
637 amounts from ground-based Pandora and MFDOAS spectrometers using the direct-sun
638 DOAS technique: Intercomparisons and application to OMI validation, *J. Geophys. Res.*
639 *Atmos.*, 114, <https://doi.org/10.1029/2009JD011848>, 2009.

640 Janjić, T., Bormann, N., Bocquet, M., Carton, J. A., Cohn, S. E., Dance, S. L., Losa, S. N.,
641 Nichols, N. K., Potthast, R., Waller, J. A., and Weston, P.: On the representation error in

642 data assimilation, *Q. J. R. Meteorol. Soc.*, 144, 1257–1278,
 643 <https://doi.org/10.1002/qj.3130>, 2018.

644 Judd, L. M., Al-Saadi, J. A., Szykman, J. J., Valin, L. C., Janz, S. J., Kowalewski, M. G., Eskes,
 645 H. J., Veefkind, J. P., Cede, A., Mueller, M., Gebetsberger, M., Swap, R., Pierce, R. B.,
 646 Nowlan, C. R., Abad, G. G., Nehrir, A., and Williams, D.: Evaluating Sentinel-5P
 647 TROPOMI tropospheric NO₂ column densities with airborne and Pandora spectrometers
 648 near New York City and Long Island Sound, *Atmos. Meas. Tech.*, 13, 6113–6140,
 649 <https://doi.org/10.5194/amt-13-6113-2020>, 2020.

650 Kendon, E. J., Roberts, N. M., Fowler, H. J., Roberts, M. J., Chan, S. C., and Senior, C. A.:
 651 Heavier summer downpours with climate change revealed by weather forecast resolution
 652 model, *Nature Clim. Change*, 4, 570–576, <https://doi.org/10.1038/nclimate2258>, 2014.

653 Kim, H. C., Lee, S.-M., Chai, T., Ngan, F., Pan, L., and Lee, P.: A Conservative Downscaling of
 654 Satellite-Detected Chemical Compositions: NO₂ Column Densities of OMI, GOME-2,
 655 and CMAQ, *Remote Sens.*, 10, 1001, <https://doi.org/10.3390/rs10071001>, 2018.

656 Laughner, J. L., Zhu, Q., and Cohen, R. C.: The Berkeley High Resolution Tropospheric NO₂
 657 product, *Earth Syst. Sci. Data*, 10, 2069–2095, <https://doi.org/10.5194/essd-10-2069-2018>, 2018.

658 Li, R., Cui, L., Meng, Y., Zhao, Y., and Fu, H.: Satellite-based prediction of daily SO₂ exposure
 659 across China using a high-quality random forest-spatiotemporal Kriging (RF-STK) model
 660 for health risk assessment, *Atmos. Environ.*, 208, 10–19,
 661 <https://doi.org/10.1016/j.atmosenv.2019.03.029>, 2019.

662 Matheron, G.: Principles of geostatistics, *Econ. Geol.*, 58, 1246–1266,
 663 <https://doi.org/10.2113/gsecongeo.58.8.1246>, 1963.

664 Mazzuca, G. M., Ren, X., Loughner, C. P., Estes, M., Crawford, J. H., Pickering, K. E.,
 665 Weinheimer, A. J., and Dickerson, R. R.: Ozone production and its sensitivity to NO_x
 666 and VOCs: results from the DISCOVER-AQ field experiment, Houston 2013, *Atmos.*
 667 *Chem. Phys.*, 16, 14463–14474, <https://doi.org/10.5194/acp-16-14463-2016>, 2016.

668 Nowlan, C. R., Liu, X., Janz, S. J., Kowalewski, M. G., Chance, K., Follette-Cook, M. B., Fried,
 669 A., González Abad, G., Herman, J. R., Judd, L. M., Kwon, H.-A., Loughner, C. P.,
 670 Pickering, K. E., Richter, D., Spinei, E., Walega, J., Weibring, P., and Weinheimer, A. J.:
 671 Nitrogen dioxide and formaldehyde measurements from the GEOSTationary Coastal and
 672 Air Pollution Events (GEO-CAPE) Airborne Simulator over Houston, Texas, *Atmos.*
 673 *Meas. Tech.*, 11, 5941–5964, <https://doi.org/10.5194/amt-11-5941-2018>, 2018.

674 Nowlan, C. R., Liu, X., Leitch, J. W., Chance, K., González Abad, G., Liu, C., Zoogman, P.,
 675 Cole, J., Delker, T., Good, W., Murcay, F., Ruppert, L., Soo, D., Follette-Cook, M. B.,
 676 Janz, S. J., Kowalewski, M. G., Loughner, C. P., Pickering, K. E., Herman, J. R., Beaver,
 677 M. R., Long, R. W., Szykman, J. J., Judd, L. M., Kelley, P., Luke, W. T., Ren, X., and
 678 Al-Saadi, J. A.: Nitrogen dioxide observations from the Geostationary Trace gas and
 679 Aerosol Sensor Optimization (GeoTASO) airborne instrument: Retrieval algorithm and
 680 measurements during DISCOVER-AQ Texas 2013, *Atmos. Meas. Tech.*, 9, 2647–2668,
 681 <https://doi.org/10.5194/amt-9-2647-2016>, 2016.

682 Onn, F. and Zebker, H. A.: Correction for interferometric synthetic aperture radar atmospheric
 683 phase artifacts using time series of zenith wet delay observations from a GPS network, *J.*
 684 *Geophys. Res. Solid Earth*, 111, <https://doi.org/10.1029/2005JB004012>, 2006.

685 Pan, S., Choi, Y., Jeon, W., Roy, A., Westenbarger, D. A., and Kim, H. C.: Impact of high-
 686 resolution sea surface temperature, emission spikes and wind on simulated surface ozone
 687

688 in Houston, Texas during a high ozone episode, *Atmos. Environ.*, 152, 362–376,
689 <https://doi.org/10.1016/j.atmosenv.2016.12.030>, 2017b.

690 Pan, S., Choi, Y., Roy, A., and Jeon, W.: Allocating emissions to 4 km and 1 km horizontal
691 spatial resolutions and its impact on simulated NO_x and O₃ in Houston, TX, *Atmos.*
692 *Environ.*, 164, 398–415, <https://doi.org/10.1016/j.atmosenv.2017.06.026>, 2017a.

693 Pan, S., Choi, Y., Roy, A., Li, X., Jeon, W., and Souri, A. H.: Modeling the uncertainty of
694 several VOC and its impact on simulated VOC and ozone in Houston, Texas, *Atmos.*
695 *Environ.*, 120, 404–416, <https://doi.org/10.1016/j.atmosenv.2015.09.029>, 2015.

696 Platt, U., Wagner, T., Kuhn, J., and Leisner, T.: The “ideal” spectrograph for atmospheric
697 observations, *Atmos. Meas. Tech.*, 14, 6867–6883, <https://doi.org/10.5194/amt-14-6867-2021>, 2021.

698 Pyrcz MJ, Deutsch CV. The whole story on the hole effect. *Geostatistical Association of
699 Australasia, Newsletter*. 2003 May;18:3-5.

700 Rennen, G.: Subset Selection from Large Datasets for Kriging Modeling, *Social Science
701 Research Network*, Rochester, NY, <https://doi.org/10.2139/ssrn.1104595>, 2008.

702 Russell, A. R., Perring, A. E., Valin, L. C., Bucsela, E. J., Browne, E. C., Wooldridge, P. J., and
703 Cohen, R. C.: A high spatial resolution retrieval of NO₂ column densities from OMI:
704 method and evaluation, *Atmos. Chem. Phys.*, 11, 8543–8554,
705 <https://doi.org/10.5194/acp-11-8543-2011>, 2011.

706 Shah, V., Jacob, D. J., Li, K., Silvern, R. F., Zhai, S., Liu, M., Lin, J., and Zhang, Q.: Effect of
707 changing NO_x lifetime on the seasonality and long-term trends of satellite-observed
708 tropospheric NO₂ columns over China, *Atmos. Chem. Phys.*, 20, 1483–1495,
709 <https://doi.org/10.5194/acp-20-1483-2020>, 2020.

710 Souri, A. H., Choi, Y., Jeon, W., Li, X., Pan, S., Diao, L., and Westenbarger, D. A.: Constraining
711 NO_x emissions using satellite NO₂ measurements during 2013 DISCOVER-AQ Texas
712 campaign, *Atmos. Environ.*, 131, 371–381,
713 <https://doi.org/10.1016/j.atmosenv.2016.02.020>, 2016.

714 Souri, A. H., Choi, Y., Kodros, J. K., Jung, J., Shpund, J., Pierce, J. R., Lynn, B. H., Khain, A.,
715 and Chance, K.: Response of Hurricane Harvey’s rainfall to anthropogenic aerosols: A
716 sensitivity study based on spectral bin microphysics with simulated aerosols, *Atmos.*
717 *Res.*, 242, 104965, <https://doi.org/10.1016/j.atmosres.2020.104965>, 2020a.

718 Souri, A. H., Choi, Y., Pan, S., Curci, G., Nowlan, C. R., Janz, S. J., Kowalewski, M. G., Liu, J.,
719 Herman, J. R., and Weinheimer, A. J.: First Top-Down Estimates of Anthropogenic NO_x
720 Emissions Using High-Resolution Airborne Remote Sensing Observations, *J. Geophys.*
721 *Res. Atmos.*, 123, 3269–3284, <https://doi.org/10.1002/2017JD028009>, 2018.

722 Souri, A. H., Nowlan, C. R., Wolfe, G. M., Lamsal, L. N., Chan Miller, C. E., Abad, G. G., Janz,
723 S. J., Fried, A., Blake, D. R., Weinheimer, A. J., Diskin, G. S., Liu, X., and Chance, K.:
724 Revisiting the effectiveness of HCHO/NO₂ ratios for inferring ozone sensitivity to its
725 precursors using high resolution airborne remote sensing observations in a high ozone
726 episode during the KORUS-AQ campaign, *Atmos. Environ.*, 224, 117341,
727 <https://doi.org/10.1016/j.atmosenv.2020.117341>, 2020b.

728 Sun, K., Zhu, L., Cady-Pereira, K., Chan Miller, C., Chance, K., Clarisse, L., Coheur, P.-F.,
729 González Abad, G., Huang, G., Liu, X., Van Damme, M., Yang, K., and Zondlo, M.: A
730 physics-based approach to oversample multi-satellite, multispecies observations to a
731 common grid, *Atmos. Meas. Tech.*, 11, 6679–6701, <https://doi.org/10.5194/amt-11-6679-2018>, 2018.

732

733

734 Swall, J. L. and Foley, K. M.: The impact of spatial correlation and incommensurability on
735 model evaluation, *Atmos. Environ.*, 43, 1204–1217,
736 <https://doi.org/10.1016/j.atmosenv.2008.10.057>, 2009.

737 Tadić, J. M., Michalak, A. M., Iraci, L., Ilić, V., Biraud, S. C., Feldman, D. R., Bui, T., Johnson,
738 M. S., Loewenstein, M., Jeong, S., Fischer, M. L., Yates, E. L., and Ryoo, J.-M.: Elliptic
739 Cylinder Airborne Sampling and Geostatistical Mass Balance Approach for Quantifying
740 Local Greenhouse Gas Emissions, *Environ. Sci. Technol.*, 51, 10012–10021,
741 <https://doi.org/10.1021/acs.est.7b03100>, 2017.

742 Tang, W., Edwards, D. P., Emmons, L. K., Worden, H. M., Judd, L. M., Lamsal, L. N., Al-Saadi,
743 J. A., Janz, S. J., Crawford, J. H., Deeter, M. N., Pfister, G., Buchholz, R. R., Gaubert, B.,
744 and Nowlan, C. R.: Assessing sub-grid variability within satellite pixels over urban
745 regions using airborne mapping spectrometer measurements, *Atmos. Meas. Tech.*, 14,
746 4639–4655, <https://doi.org/10.5194/amt-14-4639-2021>, 2021.

747 Valin, L. C., Russell, A. R., Hudman, R. C., and Cohen, R. C.: Effects of model resolution on the
748 interpretation of satellite NO₂ observations, *Atmos. Chem. Phys.*, 11, 11647–11655,
749 <https://doi.org/10.5194/acp-11-11647-2011>, 2011.

750 Vinken, G. C. M., Boersma, K. F., Jacob, D. J., and Meijer, E. W.: Accounting for non-linear
751 chemistry of ship plumes in the GEOS-Chem global chemistry transport model, *Atmos.*
752 *Chem. Phys.*, 11, 11707–11722, <https://doi.org/10.5194/acp-11-11707-2011>, 2011.

753 Wang, P., Piters, A., van Geffen, J., Tuinder, O., Stammes, P., and Kinne, S.: Shipborne MAX-
754 DOAS measurements for validation of TROPOMI NO₂ products, *Atmos. Meas. Tech.*,
755 13, 1413–1426, <https://doi.org/10.5194/amt-13-1413-2020>, 2020.

756 Wang, Y., Sabatino, S. D., Martilli, A., Li, Y., Wong, M. S., Gutiérrez, E., and Chan, P. W.:
757 Impact of land surface heterogeneity on urban heat island circulation and sea-land breeze
758 circulation in Hong Kong, *J. Geophys. Res. Atmos.*, 122, 4332–4352,
759 <https://doi.org/10.1002/2017JD026702>, 2017.

760 Wolfe, G. M., Nicely, J. M., Clair, J. M. S., Hanisco, T. F., Liao, J., Oman, L. D., Brune, W. B.,
761 Miller, D., Thames, A., Abad, G. G., Ryerson, T. B., Thompson, C. R., Peischl, J.,
762 McKain, K., Sweeney, C., Wennberg, P. O., Kim, M., Crounse, J. D., Hall, S. R.,
763 Ullmann, K., Diskin, G., Bui, P., Chang, C., and Dean-Day, J.: Mapping hydroxyl
764 variability throughout the global remote troposphere via synthesis of airborne and
765 satellite formaldehyde observations, *PNAS*, 116, 11171–11180,
766 <https://doi.org/10.1073/pnas.1821661116>, 2019.

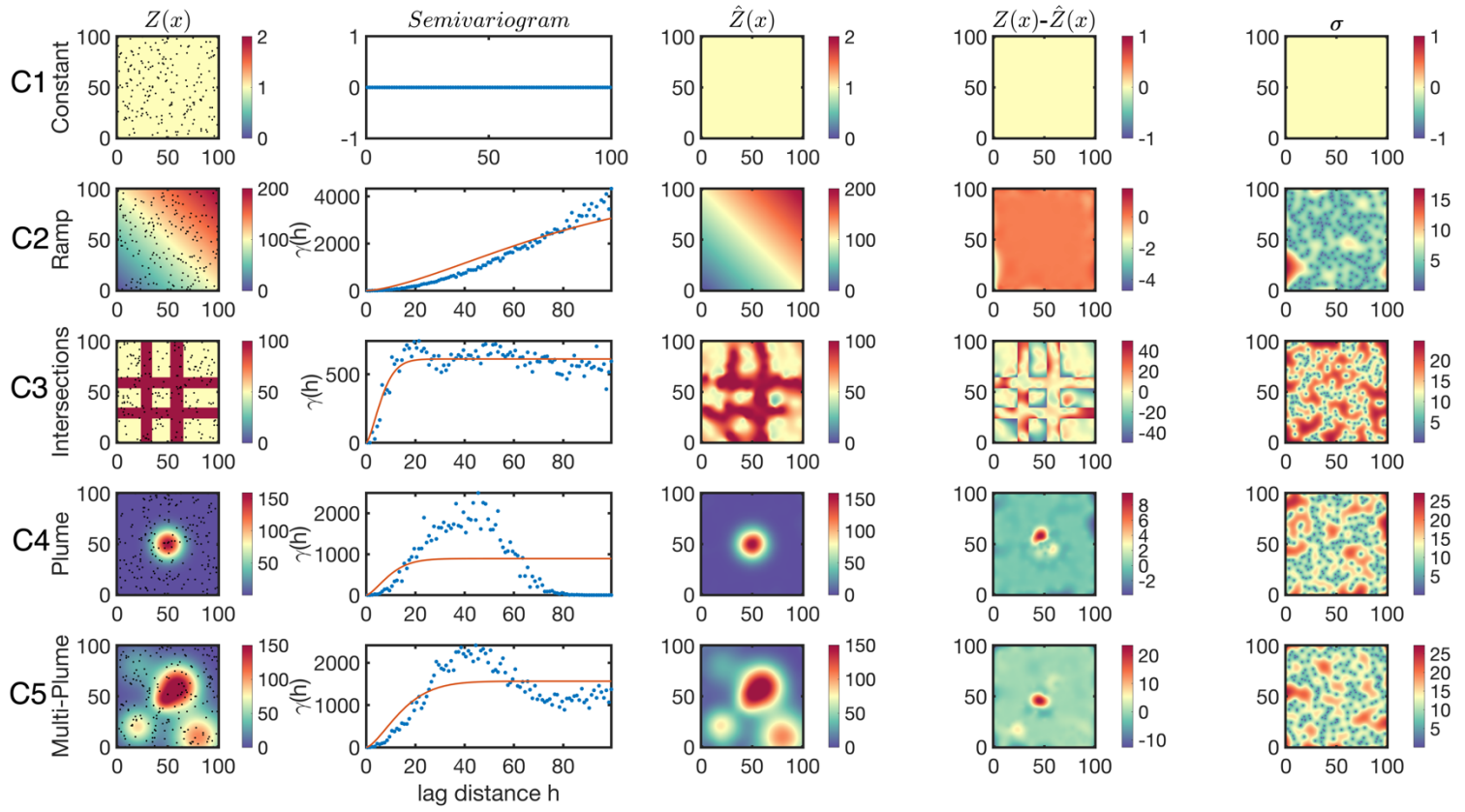
767 Wu, C.-D., Zeng, Y.-T., and Lung, S.-C. C.: A hybrid kriging/land-use regression model to
768 assess PM_{2.5} spatial-temporal variability, *Sci. Total Environ.*, 645, 1456–1464,
769 <https://doi.org/10.1016/j.scitotenv.2018.07.073>, 2018.

770 Yu, K., Jacob, D. J., Fisher, J. A., Kim, P. S., Marais, E. A., Miller, C. C., Travis, K. R., Zhu, L.,
771 Yantosca, R. M., Sulprizio, M. P., Cohen, R. C., Dibb, J. E., Fried, A., Mikoviny, T.,
772 Ryerson, T. B., Wennberg, P. O., and Wisthaler, A.: Sensitivity to grid resolution in the
773 ability of a chemical transport model to simulate observed oxidant chemistry under high-
774 isoprene conditions, *Atmos. Chem. Phys.*, 16, 4369–4378, <https://doi.org/10.5194/acp-16-4369-2016>, 2016.

775 Zhan, Y., Luo, Y., Deng, X., Zhang, K., Zhang, M., Grieneisen, M. L., and Di, B.: Satellite-
776 Based Estimates of Daily NO₂ Exposure in China Using Hybrid Random Forest and
777 Spatiotemporal Kriging Model, *Environ. Sci. Technol.*, 52, 4180–4189,
778 <https://doi.org/10.1021/acs.est.7b05669>, 2018.

780 Zhao, X., Griffin, D., Fioletov, V., McLinden, C., Cede, A., Tiefengraber, M., Müller, M.,
781 Bognar, K., Strong, K., Boersma, F., Eskes, H., Davies, J., Ogyu, A., and Lee, S. C.:
782 Assessment of the quality of TROPOMI high-spatial-resolution NO₂ data products in the
783 Greater Toronto Area, *Atmos. Meas. Tech.*, 13, 2131–2159, <https://doi.org/10.5194/amt-13-2131-2020>, 2020.
785

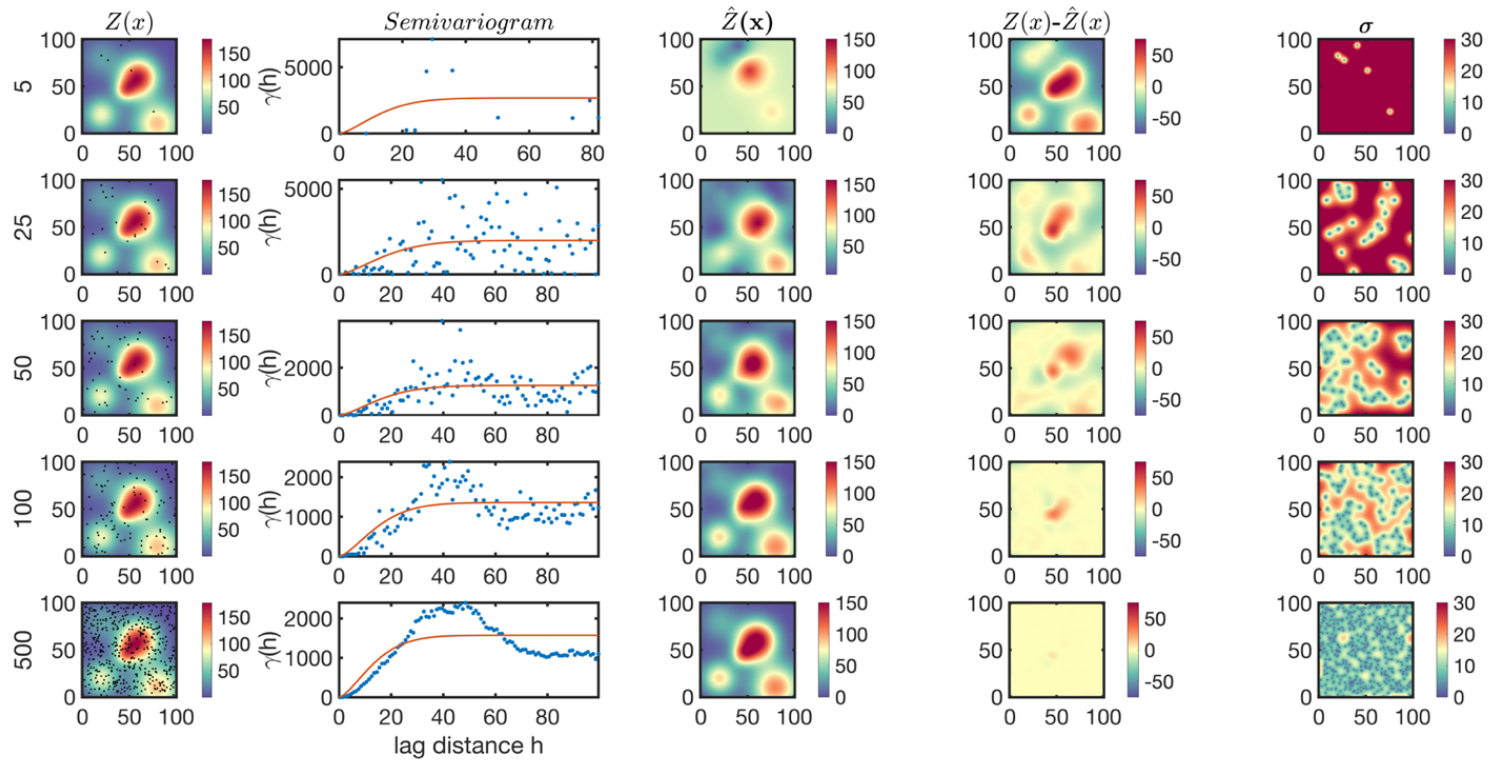
786 Figures:



788 **Figure 1.** (first column) Five theoretical fields randomly sampled with 200 points (dots), namely,
789 a constant field (C1), a ramp starting from zero in the lower left to higher values in the upper right
790 (C2), an intersection with concentrated values in four corridors (C3), a Gaussian plume placed in
791 the center (C4), and multiple Gaussian plumes spread over the entire domain (C5). (second column)
792 the corresponding isotropic semivariograms computed based on Eq.2; the red line shows the stable
793 Gaussian fitted to the semivariogram based on Levenberg-Marquardt method. (third column) The
794 kriging estimate at the same resolution of the truth (i.e., 1×1) based on Eq.6. (fourth column) The
795 difference between the estimate and the truth. (fifth column) the kriging standard error based on
796 Eq.11.

797

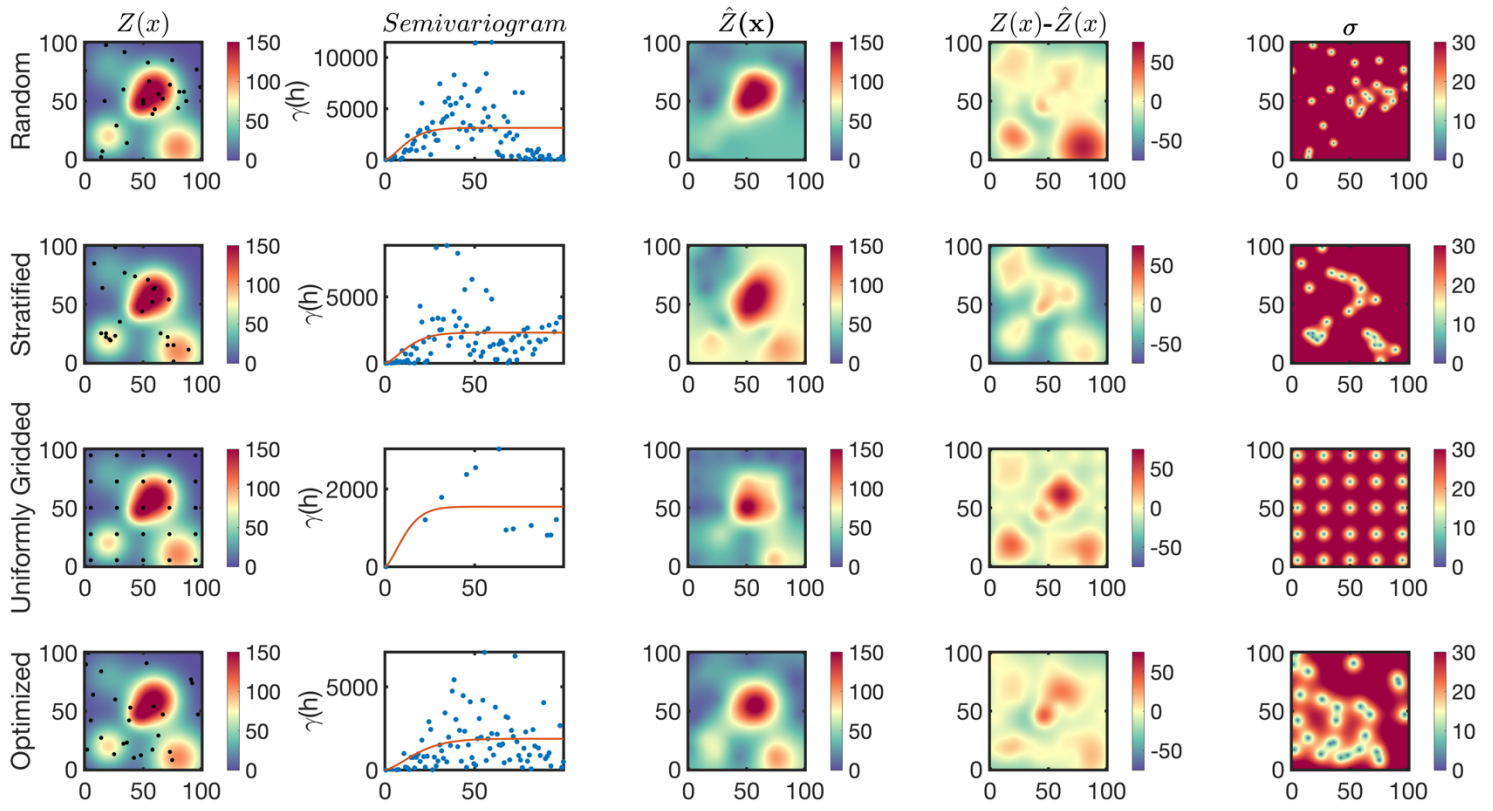
798



800 **Figure 2.** (first column) The multi-plume case (C5) randomly sampled with different number of
 801 samples (5, 25, 50, 100, and 500), (second column) the corresponding isotropic semivariogram,
 802 (third column) the kriging estimate, (fourth column) the difference between the estimate and the
 803 truth, and (fifth column) the kriging standard error.

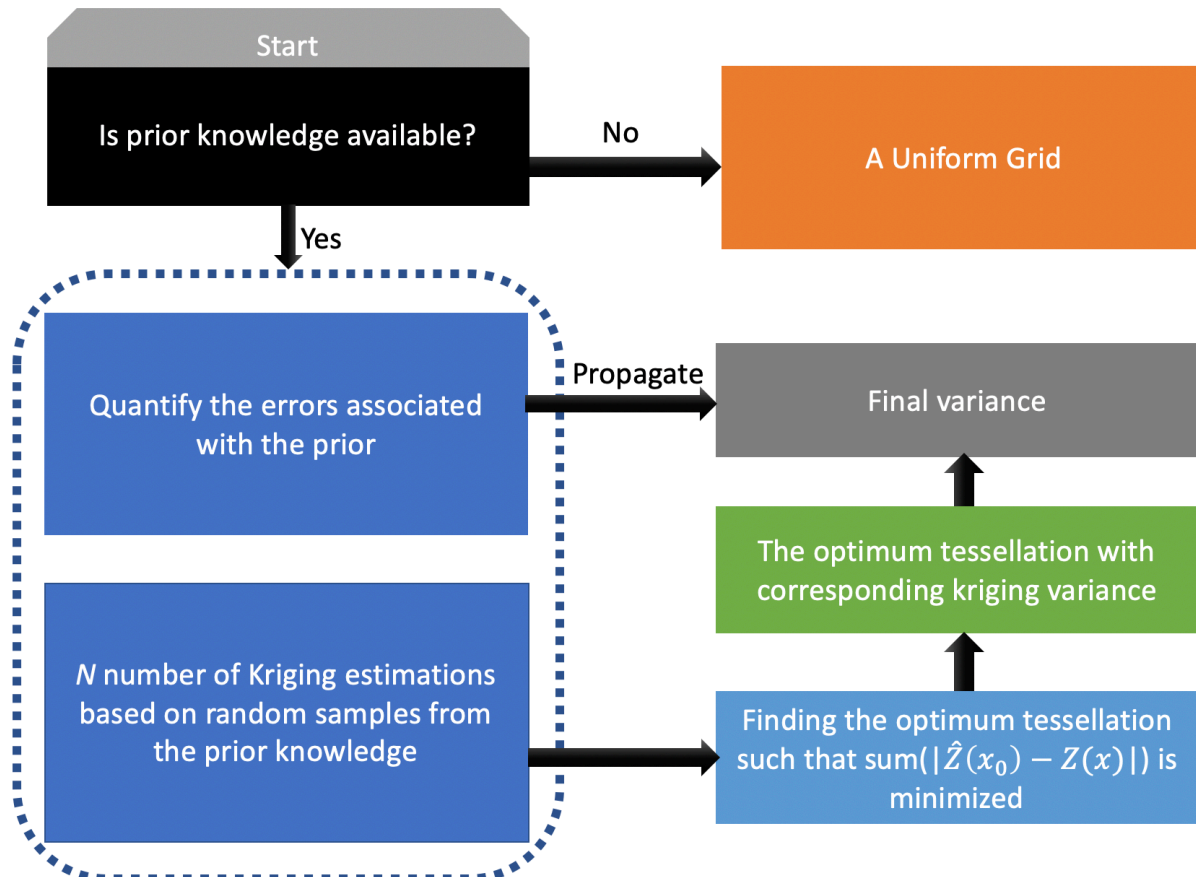
804

805



807 **Figure 3.** The multi-plume case (C5) randomly sampled by four different sampling strategies
 808 using a constant number of samples (25). The sampling strategies include purely random (first
 809 row), stratified random (second row), uniform grids (third row), and an optimized tessellation
 810 proposed based on kriging (fourth row). Columns represent the truth, the isotropic semivariogram,
 811 the kriging estimate, the difference between the estimate and the truth, and the kriging standard
 812 error.

813

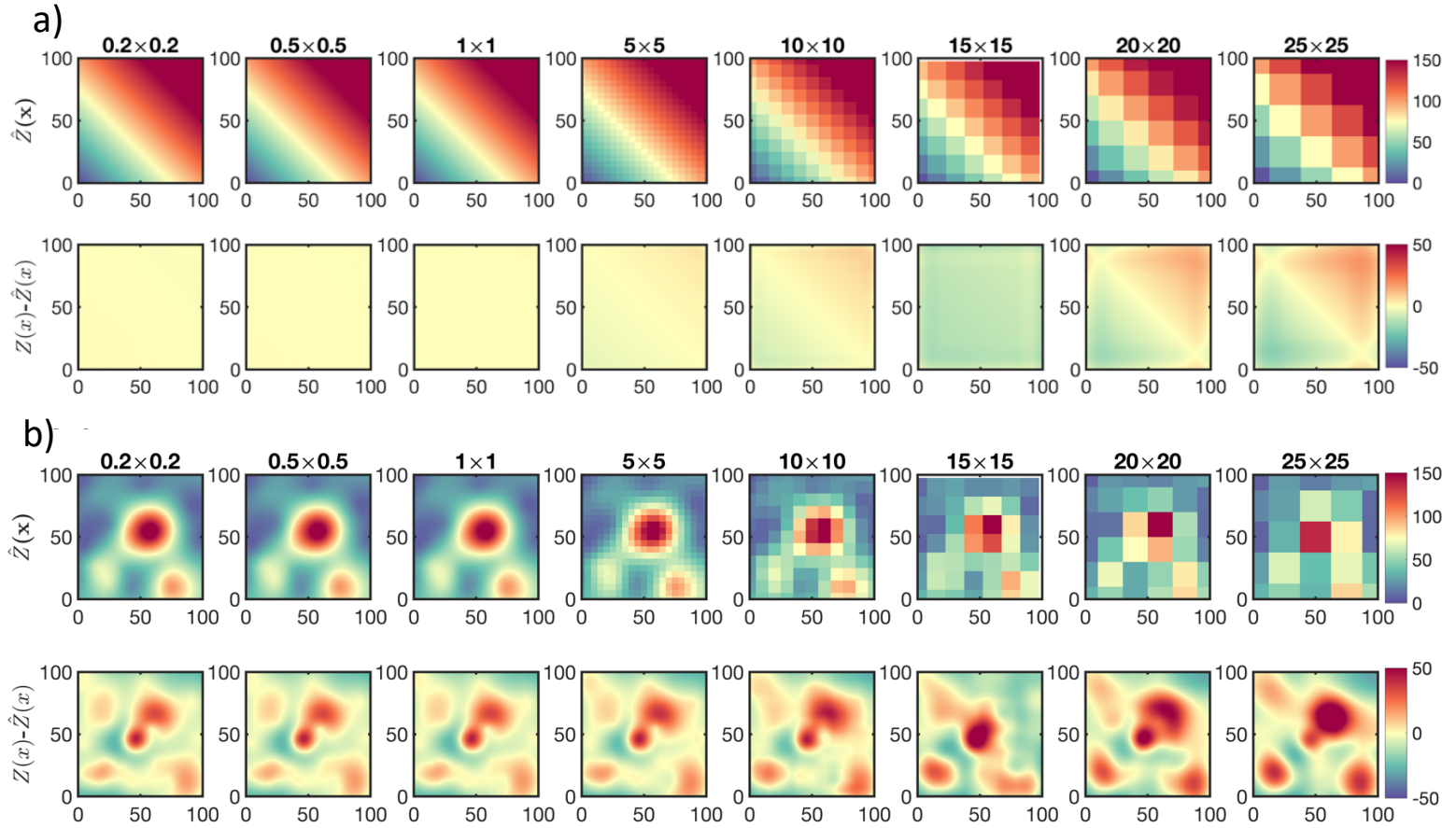


814

815 **Figure 4.** A schematic illustrating a framework for optimum sampling (tessellation) strategy. The
 816 prior knowledge refers to any data being able of describing our quantity of interest including site-
 817 visits, theoretical models, satellite observations, emissions, and etc.

818

819

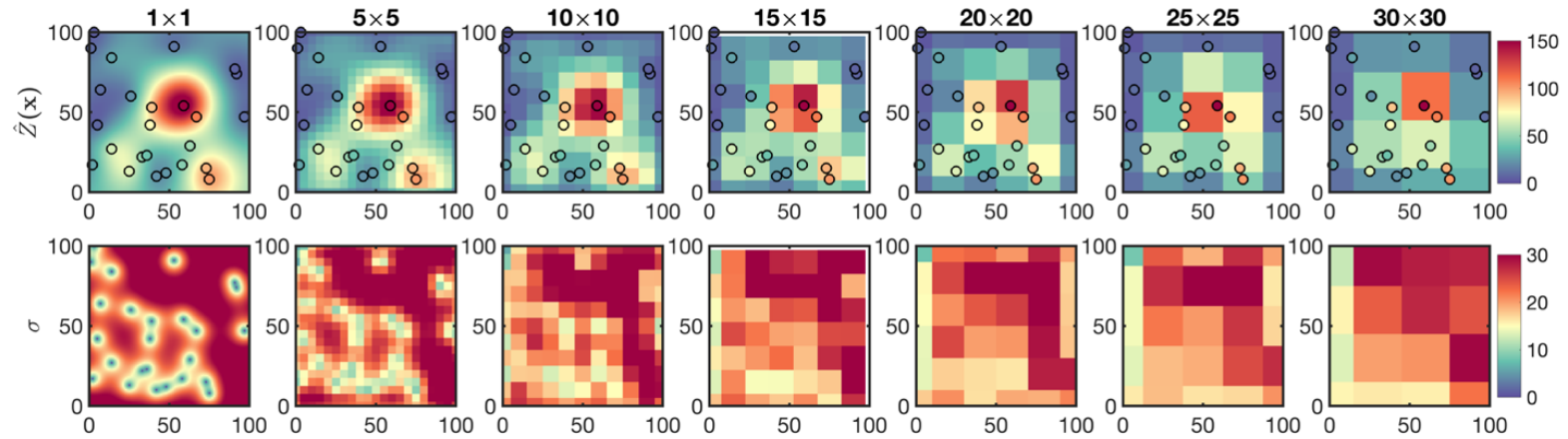


822 **Figure 5.** Finding an optimum grid size for kriging. (a) The kriging estimates of the ramp (C2) at
823 different grid resolutions ranging from 25×25 pixel to 0.2×0.2 . (b) The kriging estimates of the
824 multi-plume (C5) with optimized samples shown in Figure 3 for different grid resolutions. C2 is
825 more homogeneous than C5, as a result, it is less sensitive to the resolution of the kriging
826 estimate. The optimum grid resolution for C2 is 10×10 , whereas it is 1×1 for C5. These numbers
827 are based on observing negligible difference ($< 1\%$) between the kriging estimate at the optimum
828 resolution and the one computed at a finer resolution step. We call the optimum output for C5 as
829 C5opt.

830

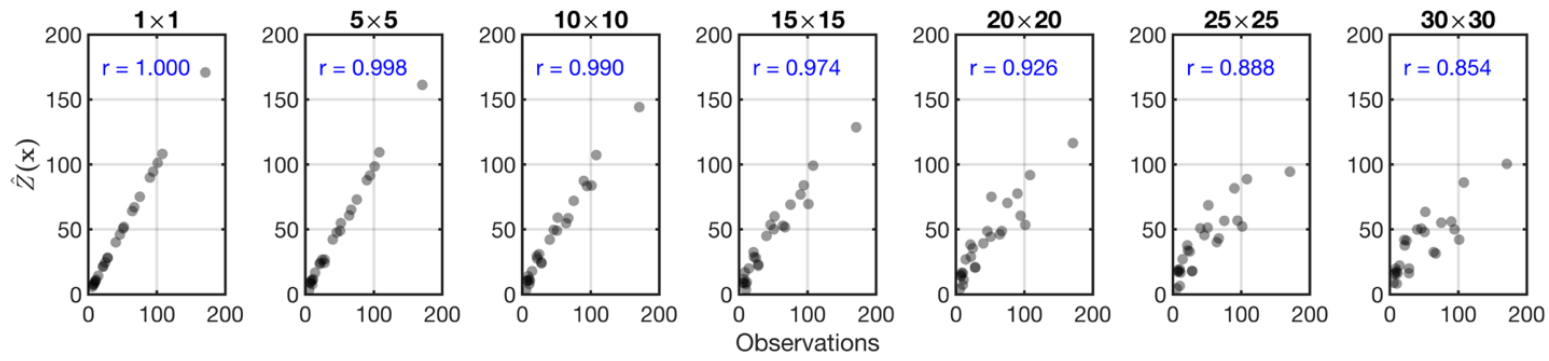
831

832



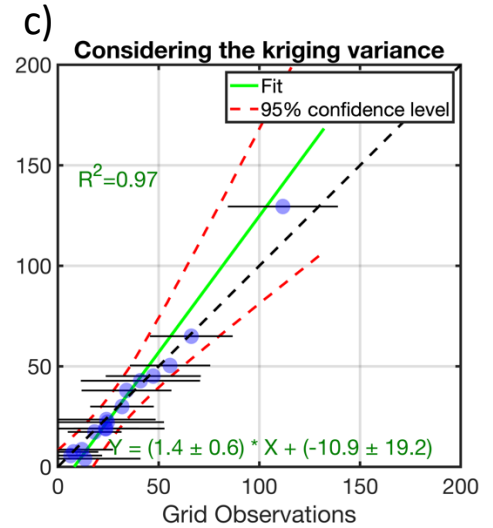
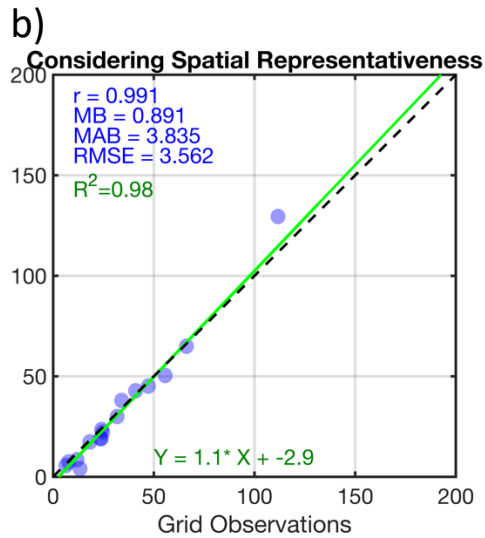
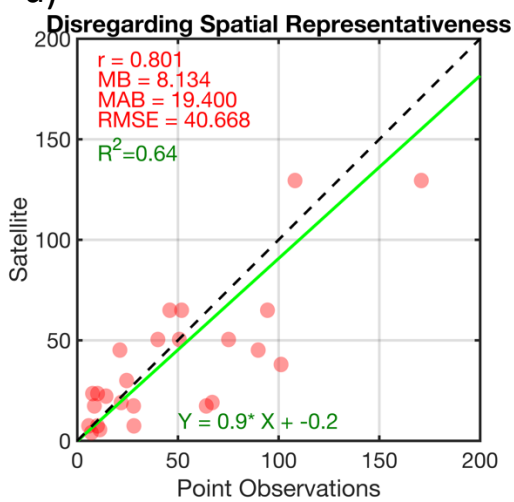
834 **Figure 6.** (first row) C5Opt outputs convolved with an ideal box kernel with different sizes (1×1
 835 up to 30×30) overlaid by the C5Opt optimum samples. (second row) the associated kriging errors
 836 convolved with the same kernel. The coarser the resolution is, the larger the discrepancy between
 837 the samples and the estimates is.

838
 839
 840
 841



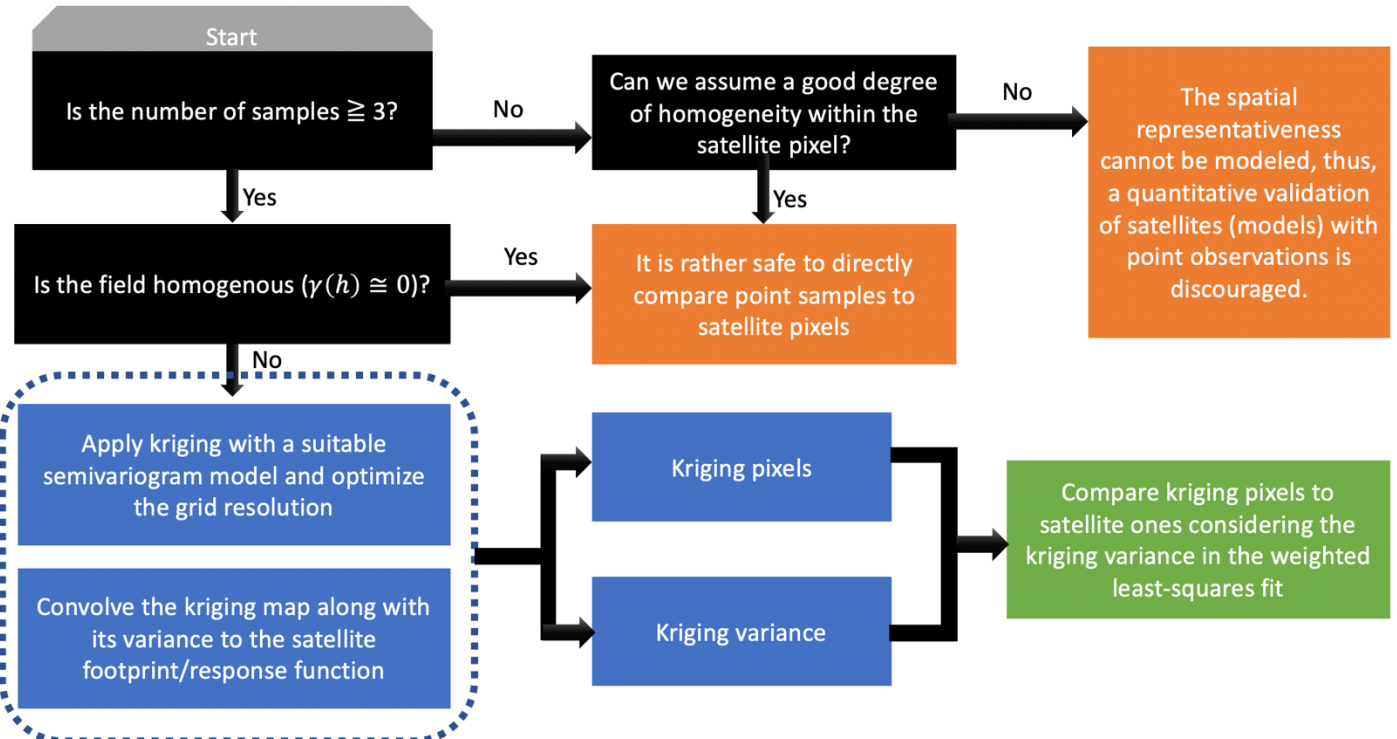
843 **Figure 7.** Illustrating the problem of spatial scale: comparisons of the kriging estimates at seven
 844 different spatial scales with the samples used for the C5opt estimation. The perceived
 845 discrepancies are purely due to the spatial representativeness.
 846

847
848
849
a)

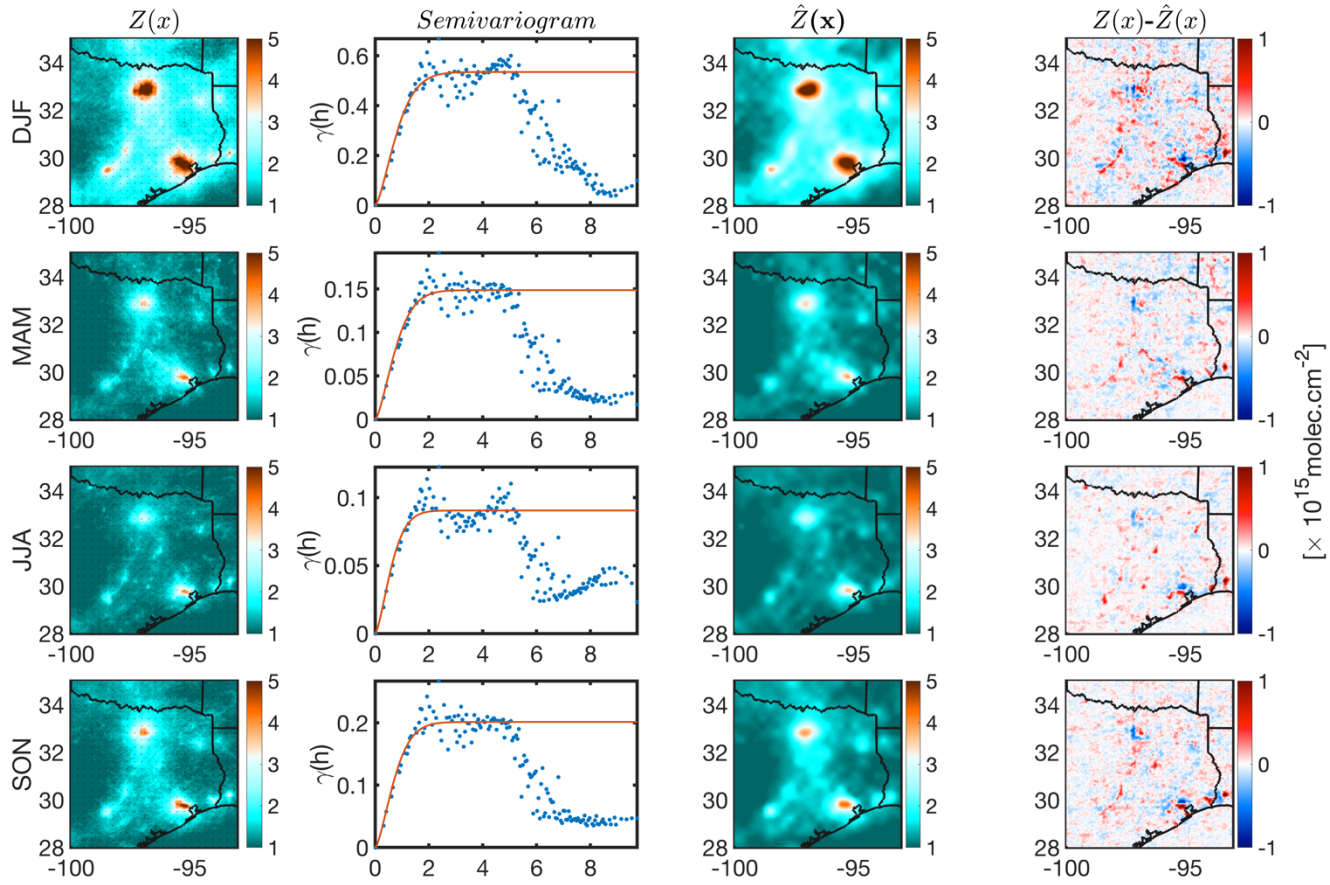


851
852
853
854
855
856
857
858
859
860

Figure 8. (a) the direct comparison of pseudo observations of a satellite observing the C5 case at 30×30 resolution versus the 25 samples used for C5opt. (b) same for y-axis, but the point samples are transformed to grid boxes using kriging convolved with the satellite spatial response function (ideal box with 30×30 kernel size). The differences in statistics between these two experiments speak to the problem of scale. (b) ignores the kriging errors but (c) incorporates them using a Monte Carlo method. Note that the best linear fit has changed indicating that the consideration of the kriging variance is critical. MB = mean bias (point minus satellite), MAB = mean absolute bias, RMSE = root mean square error, R^2 = coefficient of determination.



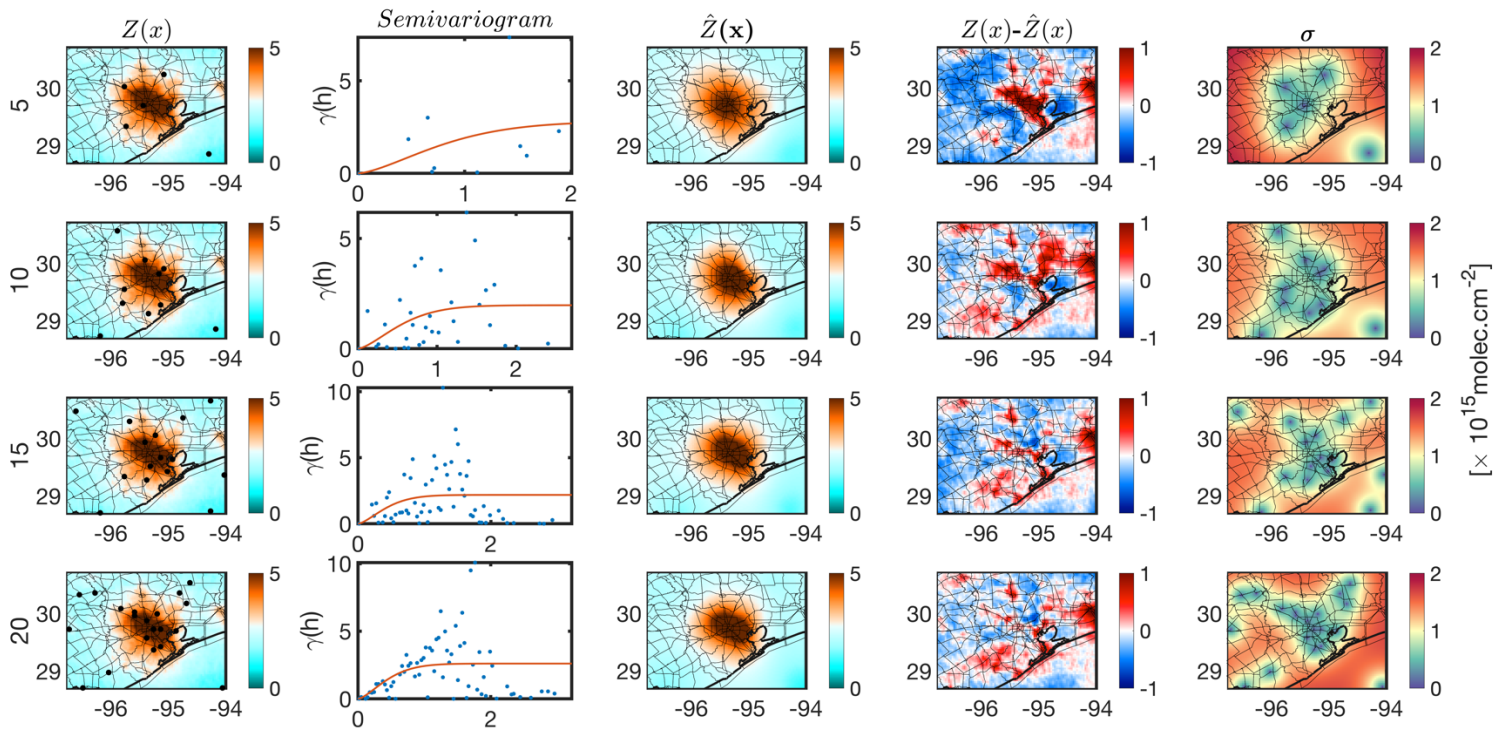
86:
862 **Figure 9.** The proposed roadmap for transforming pointwise measurements to gridded data in
863 satellite (model) validation.
864



8
 866 **Figure 10.** (first column) The spatial distribution of TROPOMI tropospheric NO₂ columns
 867 oversampled in four different seasons at 3×3 km² spatial resolution. (second column) The
 868 corresponding semivariogram from samples selected from uniform 30×30 km² blocks (shown
 869 with black dots in the first column) along the fitted stable Gaussian model (red line). (third
 870 column) the kriging estimates, and (fourth column) their differences with respect to the
 871 observations.

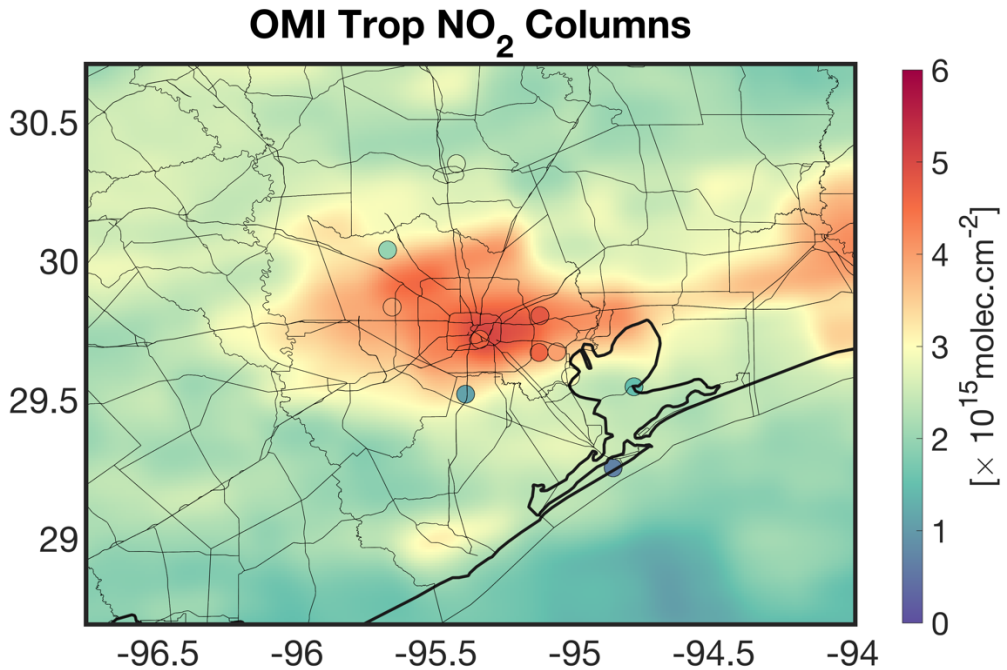
872
 873

874



876 **Figure 11.** Finding an optimum sample tessellation for wintertime over Houston given different
 877 number of spectrometers (5, 10, 15, and 20).

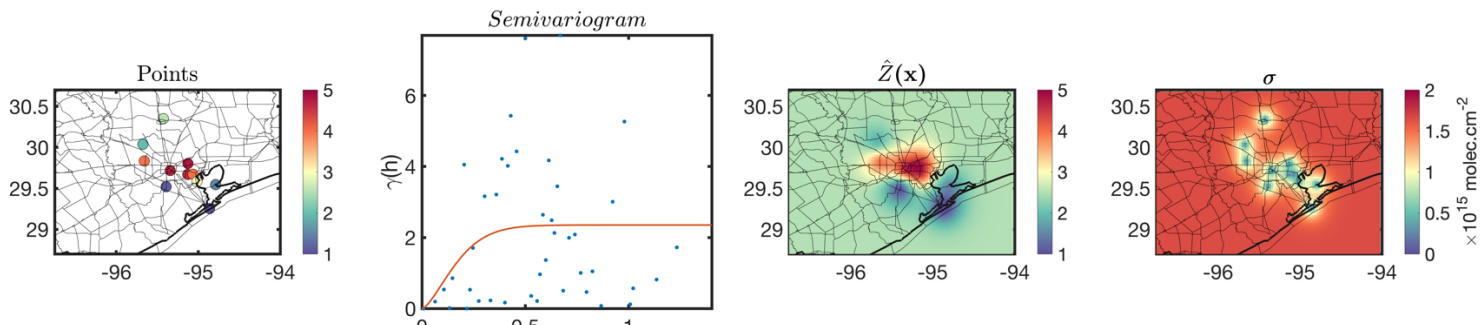
878



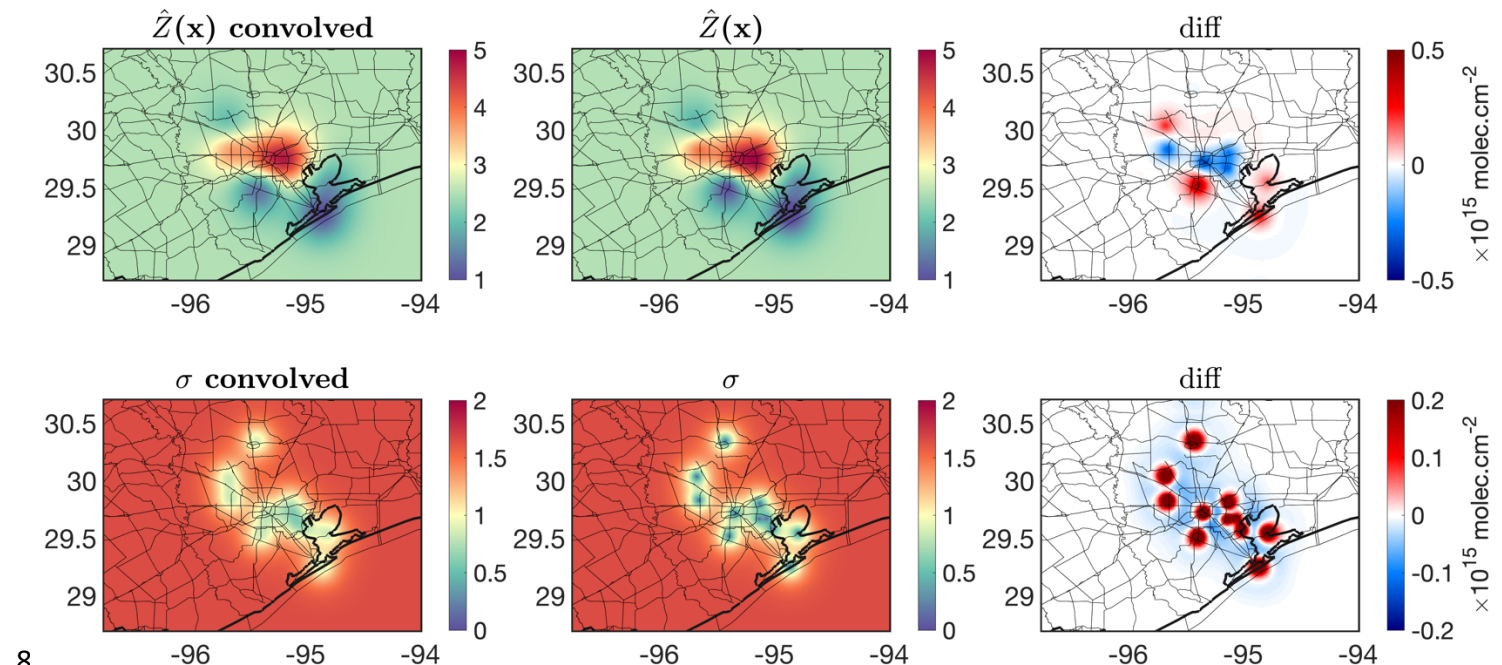
879
880

881 **Figure 12.** The spatial distribution of OMI tropospheric NO₂ columns oversampled at the resolution
 882 at $0.2 \times 0.2^\circ$ over Houston in September 2013. The plot is overlaid by surface Pandora spectrometer
 883 instrument averaged over the same month. The surface measurements originally measured the total
 884 columns, therefore we subtract the stratospheric columns provided by the OMI data ($2.8 \pm 0.16 \times 10^{15}$
 885 molecules cm^{-2}) from the total columns to focus on the tropospheric part.
 886
 887

888
889



891 **Figure 13.** The Pandora tropospheric NO₂ measurements (made from subtracting the total columns
892 from the OMI stratospheric NO₂ columns) during September 2013, the corresponding
893 semivariogram, the kriging estimates, and the kriging standard errors. Note that the semivariogram
894 suggests a large degree of spatial heterogeneity occurring at different spatial scales.
895



897 **Figure 14.** Convolving both kriging estimates and errors with the OMI spatial response function
 898 formulated in Sun et al. [2018]. The differences against the pre-convolved fields are also depicted.
 899

